March 2002 • NREL/SR-520-31754

Subcontractor Report

Search for the Factors Determining the Photodegradation in High Efficiency a-Si:H Solar Cells

Final Subcontract Report, 28 January 1998—15 August 2001

D. Han
University of North Carolina
Chapel Hill, North Carolina

National Renewable Energy Laboratory

1617 Cole Boulevard
Golden, Colorado 80401-3393

NREL is a U.S. Department of Energy Laboratory
Operated by Midwest Research Institute • Battelle • Bechtel

Contract No. DE-AC36-99-GO10337

March 2002 • NREL/SR-520-31754

Search for the Factors Determining the Photodegradation in High Efficiency a-Si:H Solar Cells

Final Subcontract Report, 28 January 1998—15 August 2001

D. Han
University of North Carolina
Chapel Hill, North Carolina

NREL Technical Monitor: Bolko von Roedern

Prepared under Subcontract No. XAK-8-17619-11

National Renewable Energy Laboratory

1617 Cole Boulevard
Golden, Colorado 80401-3393

NREL is a U.S. Department of Energy Laboratory
Operated by Midwest Research Institute • Battelle • Bechtel

Contract No. DE-AC36-99-GO10337

NOTICE

Available electronically at http://www.osti.gov/bridge

Available for a processing fee to U.S. Department of Energy
and its contractors, in paper, from:

U.S. Department of Energy
Office of Scientific and Technical Information
P.O. Box 62
Oak Ridge, TN 37831-0062
phone: 865.576.8401
fax: 865.576.5728
email: reports@adonis.osti.gov

Available for sale to the public, in paper, from:

U.S. Department of Commerce
National Technical Information Service
5285 Port Royal Road
Springfield, VA 22161
phone: 800.553.6847
fax: 703.605.6900
email: orders@ntis.fedworld.gov
online ordering: http://www.ntis.gov/ordering.htm

Printed on paper containing at least 50% wastepaper, including 20% postconsumer waste

PREFACE

This final Technical Report covers the work performed by UNC-CH for the period Jan. 28, 1998 to Aug. 15, 2001 under subcontract No. XAK-8-17619-11.

The following personnel participated in the research program:

Jonathan Baugh, Daxing Han (P.I.), Keda Wang, Lei Wu, and Guozhen Yue.
The samples were obtained from Team members at BPSolar, USSC, the a-Si group at the National Renewable Energy Laboratory (NREL) and Univ. Toledo.

Over the last three and a half years, we have benefited from numerous discussions and cooperation with our Condensed Matter colleagues at UNC-CH, Prof. L. E. McNeil, and Prof. Y. Wu. At other institutions we have collaborated with: S. Nitta and H. Habuch, Gifu, Japan, and mostly with Qi Wang, B. Nelson et al. at NREL. Our research has resulted in the publication of 27 papers and the submission of quarterly and annual reports.

TABLE OF CONTENTS

IV. EL and PL spectra From a-Si and a-SiGe p-i-n Solar Cells

LIST OF FIGURES

SUMMARY

This work is to develop improved understanding of the correlation between material properties and the amorphous silicon-based solar cell performance such as open circuit voltage, and the photodegradation. This correlation will be described in terms of photoluminescence (PL), electroluminescence (EL) and Raman spectroscopies. The other objective of this work will verify the hydrogen microstructure by nuclear magnetic resonance (NMR) technique.

Section I describes the light-induced structural changes and their correlation to conductivity changes in intrinsic a-Si:H films. Device-quality intrinsic a-Si:H films were prepared by three conditions: hot wire (HW) CVD, and plasma-enhanced (PE) CVD with and without H-dilution, which show varied light-induced conductivity changes (SWE). We found that: (a) in addition to the non-uniform H distribution, the a-Si network is inhomogeneous, (b) the light-induced increase of Si-H stretching absorption at ~2000 cm^{-1} is on the order of 10^{-2}, (c) the change of the compressive stress is on the order of 10^{-4} of the initial value in all three types of films.

Section II describes the cooperative study with NREL on transition material from a- to μc-Si using Raman, PL, optical absorption and conductivity. The films were prepared by HW CVD with varied hydrogen dilution ratios ($R=H_2:SiH_4$) from 1 to 20. The measurements demonstrated that the H-dilution in HW CVD has a much stronger effect than in PE CVD. We found: (a) At low H-dilution $R\leq 2$, there is no measurable crystallinity by Raman spectroscopy and x-ray diffraction in the a-Si:H matrix, but an optical absorption peak at ~1.25 eV appears; when R=2, the film shows the lowest subgap absorption, the highest photosensitivity, and the largest optical gap. (b) When $R\geq 3$, the c-Si phase is measurable by Raman and a low-energy PL band (0.84-1.0 eV) which appears in addition to the high-energy band (1.3-1.4 eV). Meanwhile, all the absorption spectra show a featureless lineshape. (c) An energy red-shift is observed for both PL peaks as the film grows thicker. Finally, (d) the conductivity activation energy first decreases from 0.68 to 0.12 eV, then increases as microcrystallinity increases.

In section III we first conclude that the 0.85-1.0 eV PL band originates from crystalline silicon grain boundary regions; we then studied the n-i-p solar cells near the amorphous to microcrystalline silicon transition. The study was in cooperation with National Renewable Energy Laboratory (NREL) and United Solar System Corp (USSC). By increasing either the H dilution ratio or the thickness, the i-layer structure showed a transition from amorphous to micro-crystalline silicon characterized by x-ray diffraction. The electronic states of the i-layer were examined by PL spectroscopy, which showed that: (a) below the onset of microcrystallinity, a blueshift of the 1.4 eV PL peak energy along with a decrease of the band width occur as the structural order is improved; (b) above the onset of microcrystallinity, the PL efficiency decreases by a factor of 4-5 and the PL peak energy is redshifted toward 1.2 eV as the μc-Si volume fraction is increased. In addition, the solar cell open circuit voltage shows first an increase and then a decrease, correlated with the PL peak energy position. We conclude that PL spectroscopy is a sensitive tool for characterizing the gradual amorphous-to-microcrystalline structural transition in thin film solar cells.

Section IV shows the PL and EL spectra from a-Si:H and a-SiGe p-i-n solar cells. In cooperation with BPSolar and the Univ. of Toledo, we study the effects of hydrogen dilution on a-Si:H and of varying Ge content on a-SiGe p-i-n cells by EL and PL spectroscopies. We found that (a) the EL peak energy (EL_{peak}) increased with H-dilution, correlated with an increase of open circuit voltage (V_{oc}), but the corresponding PL peak energy (PL_{peak}) did not change; and (b) that the EL_{peak} can be the same or larger than the PL_{peak}, in contrast to the usual observations. The results were explained by the model of dispersive-transport-controlled recombination for EL.

Section V shows the results of proton NMR study carried out on single a-Si:H film on quartz substrate. It is demonstrated that changes of short- and medium-range order can be detected by measuring the magnetic susceptibility χ. The result indicates that a-Si:H prepared by hot-wire CVD and plasma-enhanced CVD with high H-dilution have higher structural order compared to conventional a-Si:H.

Introduction

This report describes the research performed during the three and a half year project (Jan. 28, 1998 to Aug. 15, 2001) under NREL Subcontract No. XAK-8-17619-11. It covers mainly the most recent work.

The central unsolved problem in the study of a-Si:H is the light-induced metastability. The large light-induced conductivity changes, i.e. the SW effect is one type of the metastability, the second type, i.e. the subtle light-induced structural changes have also been observed. The metastable structual changes include the increase of Si-H absorption at ~2000 cm^{-1} on the order of 10^{-2}, and the volume expansion on the order of 10^{-5} of the initial values. Are these two types of light-induced changes linked, and how? In addition to the electronic and optical measurements, the differential infrared absorption (DIR), proton NMR and volume expansion studies of a-Si:H were carried out on both hydrogen-diluted and non-hydrogen-diluted device quality PE-CVD a-Si:H films as well as in hot-wire CVD films. The results are given in section I.

Although both the material stability and the device performance have been improved step-by-step, the microscopic origin of such metastability is still unclear. Recently, to improve stability of a-Si:H, the edge material, i.e. amorphous near and above the onset of microcrystallinity has attracted attention. However, the properties of the edge material are very sensitive not only to the deposition conditions but also to the type of the substrate and the thickness of the film. In order to better understand and then control the properties of this transition material, we carried out a systematic study using Raman, PL, optical absorption, and conductivity in a group of transition films from a- to μc-Si. Furthermore, we carried out the same measurements on n-i-p solar cells. The results are given in sections II and III.

To improve understanding of open-circuit voltage limitations of a-Si:H-based solar cells, we carry out both PL and EL measurements for groups of cells with varied (a) Ge content and (b) H-dilution ratio. The luminescence line shape and its temperature dependence are compared with the results of the cell characteristics such as V_{OC}. These results are given in section VI.

Are the light-induced conductivity changes related to overall structural ordering and/or the hydrogen microstructure of a-Si:H films? We study the overall structural order and the hydrogen microstructure using NMR techniques with the newly developed probe that allows us to study 1 μm-thick film. The structural non-uniformity is studied by the ^{1}H-NMR spectral lineshape and shift as a function of film orientation with respect to the external magnetic field.

Results

I. Light-induced Structural Changes and their Correlation to Conductivity Changes in Intrinsic Hydrogenated Amorphous Silicon Films[1-4]

I.1. Introduction

The light-induced metastable defect creation in a-Si:H, the so-called Staebler-Wronski effect (SWE),[20] has been the main problem to limit the application of a-Si:H. Much progress has been made toward understanding and reducing the metastability. There are two typical models to describe the kinetics of the light-induced DB creation: the weak-bond breaking due to carrier recombination,[21] and the metastable DB created by hydrogen collision.[22] Both models lead to the same defect creation rate equation. The weak-bond model describes the SWE as a local effect, whereas the H-collision model requires long-range H motion. These kinetics models are based on the assumption of a uniform network with one type of recombination center; i.e. neutral dangling bonds (D^o). In order to find the microscopic origin of the SWE, new techniques have been developed to study light-induced structural changes in a-Si:H films. Using the specially designed DIR technique, a light-induced reversible increase of ~1% of the Si-H absorption at wave number 2000 cm^{-1} was observed.[23] On the other hand, a light-induced expansion of 0.01% of the initial value was observed using the laser-optical cantilever-bending method (LOB).[24] Both techniques have shown that the light-induced structural changes obey the same stretched exponential rule.[23,24] Hence, the results imply that the metastable structural and conductivity (SWE) changes may share the same microscopic origin. It is worthwhile to mention that the a-Si:H films were prepared by PE-CVD with a low-H-dilution ratio of SiH_4:H_2=1:4 and at the substrate temperatures from 200-250 ˚C in both the DIR and LOB studies.

Recent calculations by Biswas[25] suggested a flipping of H to Si back-bond configuration changes the oscillator strengths of Si-H vibrations. The dipole moment of each flipped H can increase by a factor of 1.2-2. Therefore, a 10^{-4}-10^{-3} H-flip induces a 10^{-4}-10^{-3} increase in the 2000 cm^{-1} absorption. Meanwhile, the distortions of the structure induced by H flips increase the strain of the network about 10^{-4}. This H-flipping defect is suggested to occur in conjunction with the formation of metastable DBs, and the model predicts the light-induced IR absorption and volume dilation on the same orders of magnitude as observed experimentally.

a-Si:H materials with improved electronic stability have been made by using hydrogen dilution in the conventional PE-CVD,[26,27] and by HW-CVD techniques.[28] For H-diluted a-Si:H, transmission electronic microscopy (TEM) results show that the a-Si alloy is a heterogeneous mixture of an amorphous network and embedded higher ordered regions. The volume fraction of the higher ordered regions increases with increasing hydrogen dilution.[26] For device-quality HW a-Si:H, only 2-3 at.% H is needed, compared to 8-10 at.% in PE-CVD samples.[28] Furthermore, an NMR study suggests that most H atoms are highly clustered in relatively small volume fractions in HW films.[29] In the low H-content HW films, it was found that the internal friction is much smaller than in PE films.[30] This further indicates that the HW a-Si:H network has better overall four-fold coordination. Therefore, improved structural ordering could be a key factor resulting in the improvement of electronic stability. In this work, we study the light-induced structural changes in relation to the SWE behavior. Three types of device quality a-Si:H films were chosen: the HW films, and the PE-CVD a-Si:H made with and without H-dilution. Concerning the SWE, the HW films made at T_{fil} =1900 ˚C and T_S from 360 to 400 ˚C are more stable than the low H-diluted PE a-Si:H; moreover, the non-H diluted film is less stable than the H-diluted PE a-Si:H. This work aims to answer the question: if a correlation exists between the light-induced structural changes and the SWE, should the light-induced structural changes also be reduced in the HW a-Si:H films and be enhanced in the non-H diluted a-Si:H film? The experimental results yield insights into the microscopic origin of the SWE.

I.2. Samples and Experimental

Device-quality intrinsic a-Si:H films were prepared by three typical techniques, i.e. by plasma-enhanced CVD without hydrogen-dilution and with low-hydrogen-dilution at BPSolar and by hot-wire CVD techniques at NREL. The films were examined by x-ray, Raman and PL, and found to be fully amorphous, without microcrystallinity. The defect density was $\leq 10^{16}$ cm^{-3} for all the samples studied. The measurements of light-induced structural changes were carried out with help of the investigators using the DIR and LOB techniques in their laboratories. Experimental details can be found elsewhere.[1-4,23,24]

Table I. Sample preparation conditions and parameters for H microstructure studies

Sample ID	Deposition method	Substrate temperature (°C)	Reaction gas	Growth rate (Å/sec)	Film thickness (μm)	H content, C_H (at.%)
#1	HW-CVD	410	pure silane	8	~7	~1
#2	PE-CVD	200	13:1 H-diluted	1	~4	8
#3	PE-CVD	200	pure silane	4	~5	12

Table II. HW films preparation conditions and parameters for LOB studies

Sample ID	Substrate temperature (°C)	Filament current (A)	Growth rate (Å/sec)	Film thickness (μm)	H content, C_H (at.%)
TH287	280	14	7.5	~1	7
TH286	320	14	8.0	~1	5
TH185	360	15	8.0	~1	3
TH186	400	15	8.3	~1	2
TH188	440	15	11	~1	<1

Table III. H distribution parameters from NMR spectrum

Sample	Broad Linewidth (kHz)	H-H separation in clustered phase (Å)	Narrow Linewidth (kHz)	H-H separation in dilute phase (Å)	Ratio Narrow: Broad	Dilute H absent volume fraction
#1	45	1.7	3.0	9	31:69	~80%
#2	35	1.9	3.9	7	34:66	20-30%
#3	40	1.8	4.0	7	15:85	20-30%

For the differential infrared absorption measurements, a-Si:H films were deposited on intrinsic crystalline Si wafers (ρ >100 Ω-cm). In order to eliminate interference effects, the silicon wafers were single-side polished and the a-Si:H film was deposited on the rough side. The sample preparation conditions, thickness, and hydrogen contents are listed in Table I. DIR absorption spectra were measured by a home-made spectrometer. The sensitivity of the DIR instrument is about two orders of magnitude higher than the commercially available IR instruments. This allows detection of the subtle changes of the IR absorption in 5 μm thick a-Si:H film. The DIR measurements focused on the wave number range from 1800 cm^{-1} to 2300 cm^{-1} where the characteristic peak of the Si-H stretching vibration mode is located. State A was reached by annealing the initial state of the sample at 160 °C in vacuum to remove surface absorption and metastable defects. The measurements were then carried out after step-by-step light-soaking by a 90 mW/cm^2 white light with an infrared cut-off filter. Finally, the sample was annealed at 200 ˚C in vacuum for one hour to check the reversibility.

For the LOB studies, 1.0-μm thick a-Si:H films were deposited on 100 μm thick 2×20 mm^2 flat quartz substrates by hot-wire CVD. The films were also deposited on 7059 glass and crystalline-silicon substrates for conductivity and H content measurements. The sample preparation conditions, thickness,

and hydrogen contents are listed in Table II. The film-quartz system bends due to both the film volume stress during the growth process and the difference in the thermal expansion coefficients of the film and the substrate. In the LOB measurements, the detection limitation was $5x10^{-6}$ rad, which corresponds to a small displacement at the edge of the sample ~ 70 Å. This allows us to detect ~ 0.01 MPa of stress in the a-Si:H films. One piece of the quartz substrate without a-Si:H film was used as the zero-bending reference. The samples were light soaked using a 300 mW/cm^2 white light, and were then annealed at 200 ˚C for 1 h. Both the light-soaking and annealing were done in-situ. We note that the light-soaking source was 3.3 times stronger than that used in the DIR studies. The photoconductivity (PC) degradation and conductivity activation energy measurements were carried out for the films deposited on 7059 glass.

Three films, identical to #1, #2 and #3, were prepared for NMR studies. The ^{1}H NMR spectra were measured using a simple one-pulse technique and recording the subsequent free-induction decays. The home-built ^{1}H NMR probe was thoroughly cleaned and found to have a low relative ^{1}H background signal. The NMR experimental details can be found elsewhere.[16.29]

I.3 Results

1.3.1. H microstructure measured by IR and NMR:

It is generally believed that the metastability phenomenon is related to H in a-Si:H. In order to compare the H microstructure in the three device-quality a-Si:H films made by different techniques, the H configuration and its distribution were measured by IR absorption and NMR spectroscopies, respectively. Figure 1(a) shows the IR absorption spectra for samples #1, #2, and #3 listed in Table I measured by a commercial IR instrument. The top curve for #1 HW film was enlarged 5 times. The C_H content deduced from the Si-H bending mode at 630 cm^{-1} is 1, 8, and 12 at.% for samples #1,#2, and #3, respectively. In Fig. 1a, only the 630 cm^{-1} bending and the 2000 cm^{-1} stretching mode of the Si-H bond can be resolved for samples #1 and #2.

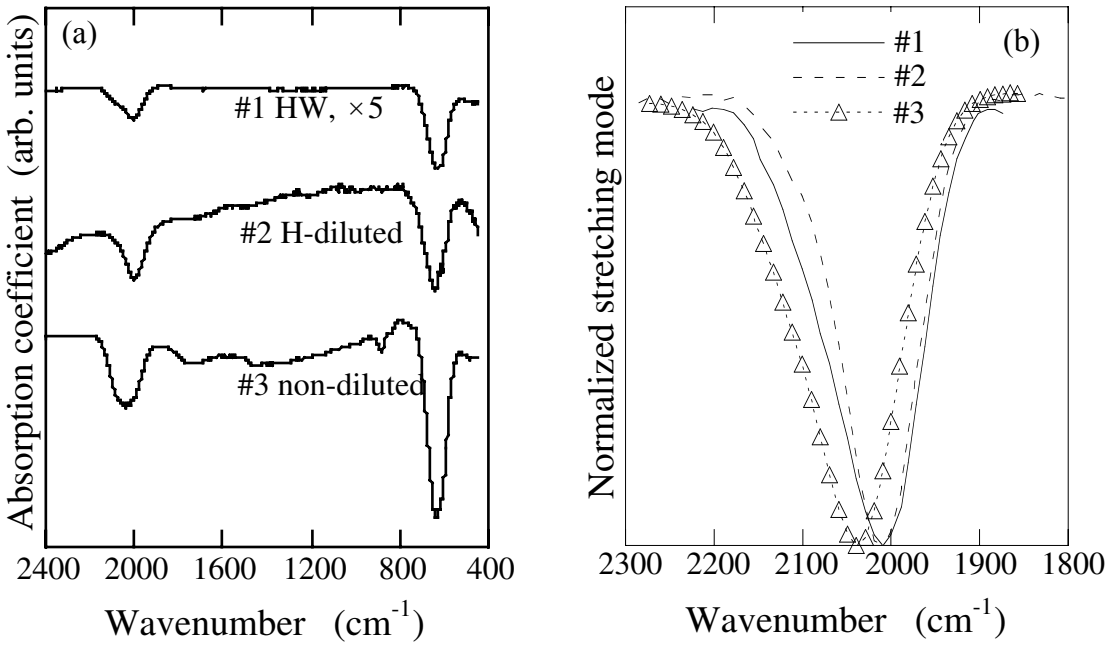

Figure 1. (a) IR spectra, and (b) the normalized stretching mode, for the HW, the H-diluted PE, and the non-H-diluted PE a-Si:H films, #1, #2 and #3.

For the non-H diluted film #3, a small 890 cm^{-1} absorption peak from the bending mode of the Si-H_2 configuration can be seen. Meanwhile, the broad absorption peak centered at 2040 cm^{-1} could be a combination of the stretching mode absorption of Si-H and Si-H_2.

In Fig. 1(b), we show the absorption coefficient of the stretching mode measured by the home-made spectrometer. The data agree well with the IR spectra in Fig. 1 (a). The broad peak of #3 could be deconvoluted into two Gaussian functions peaked at ~2010 and 2080 cm^{-1} related to the Si-H and SiH_2 stretching modes, respectively. However, one can not distinguish by IR spectroscopy whether the Si-H bonds are clustered or isolated.

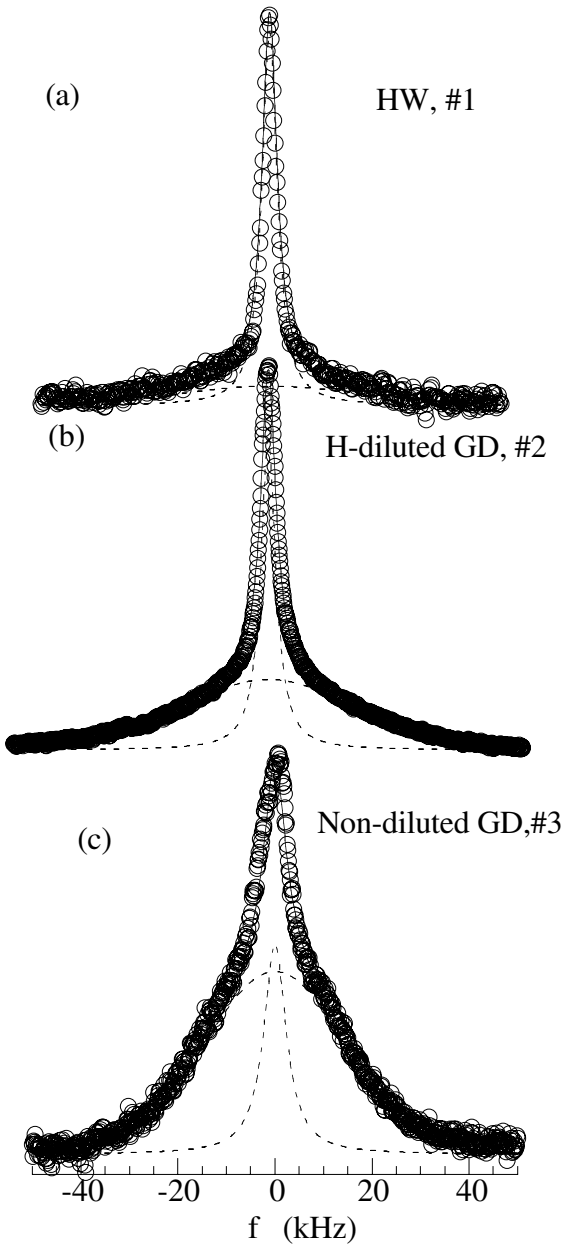

Figure 2. NMR spectra for the HW, the H-diluted PE, and the non-H-diluted PE a-Si:H samples.

The H spatial distribution was clarified by NMR measurements, as shown in Fig. 2. NMR spectra for the films prepared at the same conditions as those in Fig. 1 are shown in Fig. 2. Curves a, b, and c correspond to samples #1, #2, and #3 respectively. The spectra are fit well by a Gaussian function for the broad peak and a Lorentzian function for the narrow peak which represent clustered and isolated H environments, respectively. The area under each curve is proportional to the total number of ^1H spins contributing to the signal producing the curve. Thus, the ratio of areas of the narrow to broad peaks gives the relative amount of H in the isolated versus the clustered phase. The linewidths and the intensity ratios of narrow to broad components are listed in Table III. Despite the large difference in H contents of the HW and the H-diluted PE films, the ratio of isolated to clustered H is nearly the same in samples #1 and #2. On the other hand, the non-diluted film #3 contains much more clustered H. Furthermore, the linewidth of the broad peak is a measure of the average compactness of the clusters; i.e. a larger width means a smaller average nearest neighbor distance. The broad line of the HW sample #1 has the largest width, ~45 kHz, compared to ~37 kHz for the two PE samples #2 and #3. This indicates that the HW film has the most tightly compacted H clusters. The narrow lines are about 3-4 kHz in all the samples. The H-H nearest neighbor separations for both the clustered and the isolated phase are also given in Table III. Interestingly, we found that a 20-80% volume fraction contains nearly no isolated H in all the samples. This implies that there is an inhomogeneity of the backbone amorphous silicon network, in addition to the inhomogeneity of the H distribution. More interestingly, the HW sample #1 shows the largest volume fraction (80%) that is H-poor. Therefore, in the sense of the a-Si:H network homogeneity, the PE is better than the HW films.

However, we have found that the HW film's H distribution can be made more homogenous if the deposition conditions are optimized such as samples H610 and H777 prepared with 16 A filament current and substrate temperature of 370 ˚C. In such a case, the NMR spectra show a higher percentage of H (~45%) in the isolated phase.[31]

The above IR and NMR results show that despite the large difference in H content in the H-diluted PE and the HW samples, the hydrogen configurations and distribution are qualitatively similar. Furthermore, the tightly compacted clusters and the large H-poor volume fraction of ~ 80% in the HW film indicates improved structural ordering, but also a large structural inhomogeneity of the HW film. In contrast, the non-H-diluted sample contains $Si-H_2$ and shows more clustered Si-H as well. The next relevant question is: how does the H microstructure change upon light-soaking in these three films? If there is simple a correlation between the light-induced increase of Si-H absorption and the SWE, the DIR signal should be largest in the non-diluted PE sample #3, and smaller in the HW sample #1 compared to the H-diluted sample #2. The results are given in the next section.

1.3.2 Light-induced changes of the Si-H absorption:

State A was reached by 160˚C annealing of the initial state of the sample in vacuum. The measurements were then carried out after step-by-step light-soaking by a 90 mW/cm^2 white light for about one hundred hours. In Fig. 3, we show the saturated curve and intermediate curves of the DIR spectra; (a), (b) and (c) correspond to samples #1,#2 and #3, respectively. One can see in Fig. 3 (a) and (b) that the saturated values show an increase of about 1% of the absorption near 2000 cm^{-1} upon light-soaking for both the H-diluted and the HW films. This is quantitatively consistent with the results by Zhao et al. for low H-diluted PE a-Si:H films. For the non-diluted PE sample #3, the light-induced change is complex, including a decrease near 2040 cm^{-1} and an increase centered at 1880 cm^{-1}. Indeed, there was only a decrease centered at 2025 cm^{-1} after 30 h of light-soaking. It is possible that there is a combination of the increase at ~2000 cm^{-1} due to the metastable changes of Si-H and a decrease at a higher wavenumber due to the metastable changes related to the $Si-H_2$ bonds. For instance, we obtain the fitting curve as the solid line shown in Fig. 3(c) by using two Gaussian functions, if we assume a 1% increase at ~2000 cm^{-1} and a 1.5% decrease at 2025 cm^{-1}. Finally, the sample was annealed at 200 ˚C in a vacuum for one hour to remove the photo-induced changes. We observed an 80-90% recovery of the DIR spectrum for all samples. The lack of full recovery could be due to inhomogeneity of the film.

We found that only in some films [23], the number of metastable dangling bonds (DB) measured by constant photoconductivity method (CPM) follow the same kinetics as the change in DIR. The other films such as #1 and # do not show clear correlation of the DIR changes with the SWE kinetics.

It is expected that the DIR increase at~2000 cm^{-1} may be less in the HW- than in the PE-CVD film. It was somewhat surprising that the DIR data shows the same order of magnitude metastable increase at ~2000 cm^{-1} occurring in these three types of films. It is clear that there are light-induced IR absorption changes in these three films but the correlation with the SWE is not simple. The non-H-diluted PE film shows an additional decrease of the DIR signal at the higher wavenumber. To further study how the metastable structural changes are correlated to the electronic stability, we show another type of light-induced structural metastability in the next section.

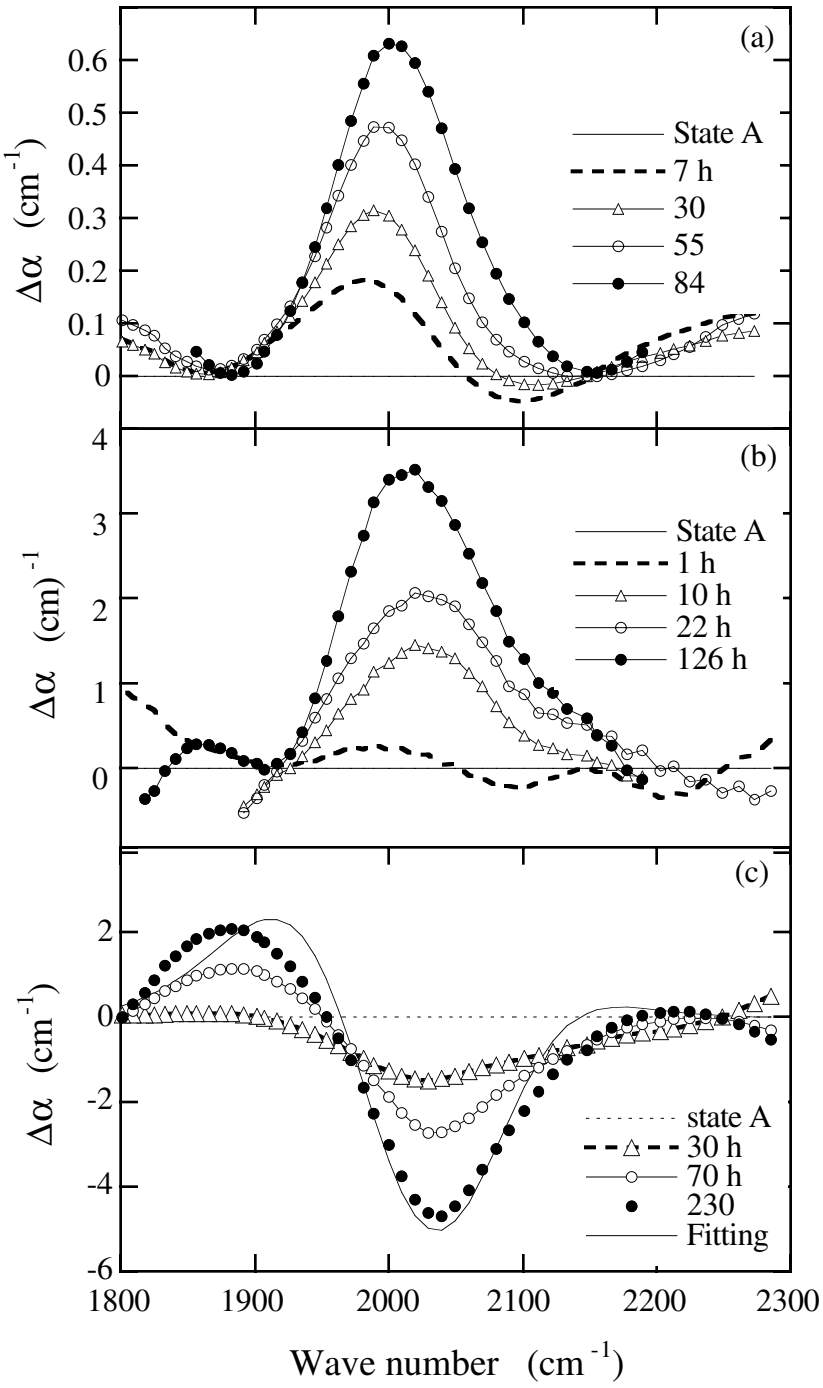

Figure 3. Light-induced changes of IR absorption measured by the DIR technique. (a), (b), and (c) correspond to samples #1,#2, and #3, respectively.

1.3.3 Initial and light-induced stress in HW a-Si:H:

Using a sensitive bending technique, a subtle film expansion was found in PE a-Si:H films upon light soaking and the kinetics of the light-induced structural change was identical to the kinetics of the SWE. We performed the same measurements at the same laboratory on a group of HW a-Si:H films that are listed in Table II. Fig. 4(a) shows the initial stress of the HW a-Si:H films as a function of both the substrate temperature T_S and the hydrogen content. The H content was deduced from the IR absorption

spectra. In Fig. 4(a), it is seen that the maximum initial compressive stress, ~425 Mpa, corresponds to a relatively low deposition temperature, T_S= 280 ˚C, and high hydrogen content, ~8 at.%. As the deposition temperature increases, both the hydrogen content and the compressive stress decrease. The minimum compression of ~74 Mpa occurs at a high deposition temperature of T_S = 440 ˚C and a low hydrogen content of ≤1 at.%. This indicates that the higher the concentration of Si-H bonds, the higher the compression of the film, since we know that Si-H bonding is the dominant H configuration in the film. Fig. 4(b) shows the photo-induced changes of the stress after a 300 mW/cm^2 light soaking for 3 hours in the same group of hot-wire a-Si:H samples. Similar to the observation in PE films, the saturated light-induced expansion is on the same order of 10^{-4} of the initial stress, and the light-induced expansion decreases with hydrogen content in the same manner as the initial compression does. The light-induced volume expansion was reversed by thermal annealing at 200 ˚C for 1 hr. We have seen that both the initial compression and the light-induced volume expansion are proportional to the Si-H bond concentration in the HW a-Si:H. And the light-induced stress in the HW a-Si:H shows as much as that in the PE-CVD films.

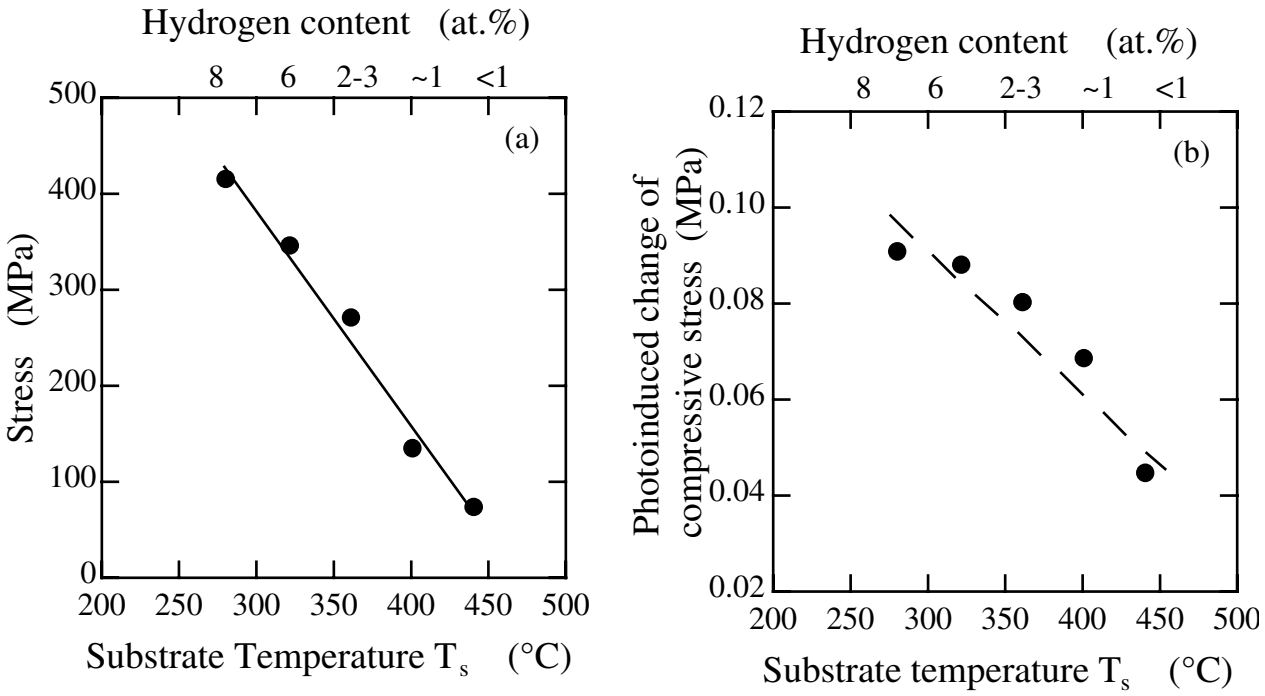

Figure 4. (a) Initial compressive stress and (b) photo-induced changes of the stress, after a 300 mW/cm^2 light soaking for 3 hours, as a function of substrate temperature and H content in a group of HW a-Si:H samples.

1.3.4 Photoconductivity degradation and metastable defects in HW a-Si:H:

The photoinduced changes in both photo- and dark- conductivities were measured for the same group of films investigated by the stress studies. The same light source for light-soaking was used for the PC measurements. In Fig. 5 we show the PC decay as a function of light-soaking time. We can see that up to 15 hr light-soaking by a 300 mW/cm^2 white light causes the PC to decrease by about one order of magnitude for the films deposited at T_S = 280 and 320 ˚C, but a smaller decrease occurs for the films deposited at T_S ≥360 ˚C. Meanwhile, the temperature dependence of the dark conductivity was measured from room temperature up to 150 ˚C before and after light-soaking. The value of the dark conductivity depends on the deposition the deposition conditions, especially the substrate temperature.

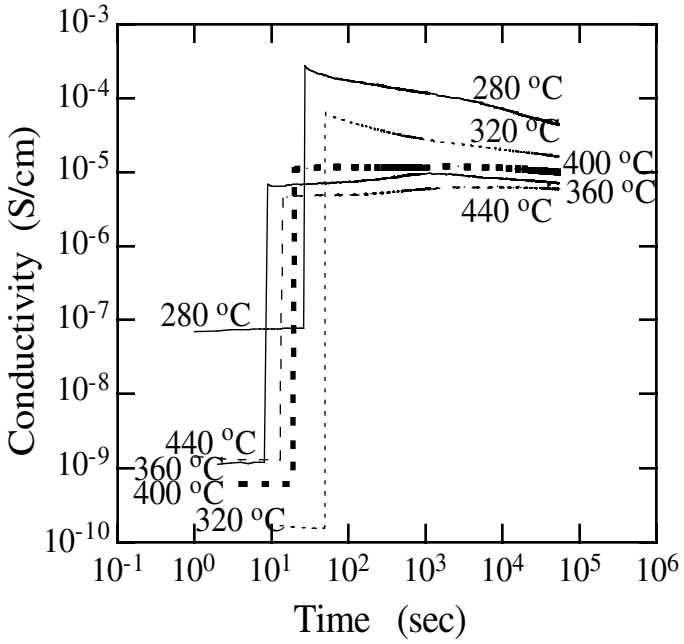

Figure 5. Photoconductivity as a function of light-soaking time for the HW samples of Fig.4.

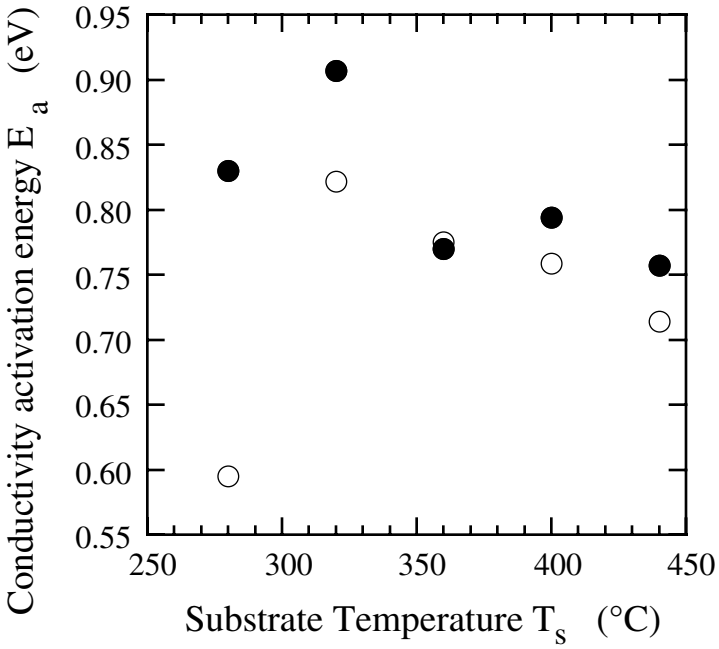

Figure 6. Conductivity activation energy before (○) and after (●) light-soaking for the samples of Fig. 4.

The position of the Fermi level is deduced from the thermal activation energy of the conductivity shown in Fig. 6. Comparing the results in Figs 5 and 6, one finds that when the Fermi level moves down quite a bit (from 0.60 to 0.83 eV and from 0.82 to 0.90 eV below the conduction band edge for the films deposited at T_S = 280 and 320 ˚C, respectively) the PC decreases by a factor of 10; otherwise, the PC-degradation effect is very small (in the films deposited at $T_S \geq 360$ ˚C). Nevertheless, none of the PC degradation curves obey the stretched-exponential law[23,24,32] described by the existing models. We noticed that

typical values of the activation energy in HW films are not only larger than that in PE films (~ 0.6 and 0.75 eV at States A and B, respectively), but are also non-reproducible during light-soaking-annealing cycles. In many cases, the activation energy is 0.9 - 1.0 eV in State A; i.e. the Fermi-level positions is located at or below mid-gap. The Fermi-level then either moves upwards or does not change upon light-soaking. After annealing a second time, the activation energies are smaller than that measured in State A, usually about 0.7 - 0.8 eV.

One may argue that the defect density of states (DOS) is a better characterization of the electronic stability. To deduce the defect density of states, the subgap absorption was measured by photo-thermal deflection spectroscopy (PDS) for the same group of HW films. We plot the results of PDS before light soaking in Fig. 7(a). We found that the sub-band gap absorption, α_{ex} , is one to two orders of magnitude higher than that in device-quality films. Unexpectedly, the 360 ˚C film shows the highest sub-band gap absorption, which could correspond to a defect density $\geq 10^{18}/cm^3$ deduced from the relation $N_d = 7.9\times10^{15}\int\alpha_{ex}\, dE$. From our previous studies by both the CPM and electron spin resonance (ESR), we know the defect density is $<10^{16}/cm^3$ in the film deposited at 360 ˚C.

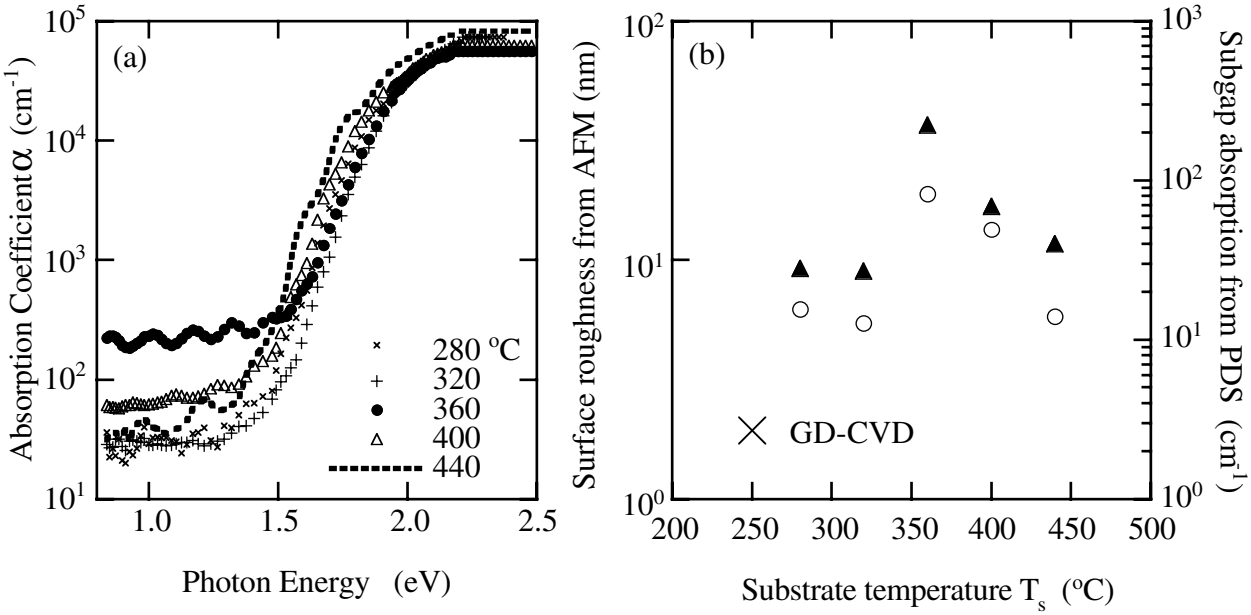

Figure 7. (a) Sub-band gap absorption and the absorption edge measured by PDS, and (b) correlation of PDS (solid triangles) with AFM (open circles) data shows the subgap absorption signal is due to surface roughness for the HW a-Si:H films as the same as in Fig. 4. An AFM data point from a PE-CVD film is also shown (x).

A possible reason for this discrepancy could be the high sensitivity of the PDS technique to surface roughness. Accordingly, we examined the film surface morphology by AFM, and plot both the PDS and AFM results as a function of film deposition temperature in Fig. 7(b). The AFM result from a PE sample is also indicated. The surface roughness was defined by an average in a scanning area of $1\times1\ \mu m^2$. A typical value of surface roughness for PE a-Si:H is 2-3 nm. On the other hand, we found that the roughness of these HW films was in the range of 5 -19 nm. Fig. 7(b) shows that there is clearly a correlation between the PDS and the AFM data, and hence the sub-band gap absorption signal from PDS is most likely due to surface roughness and not the bulk defect density for the HW a-Si:H films. The detailed mechanism of the high PDS value remain unclear. Because of the high value introduced by the surface roughness, after light-soaking there were no visible changes of the subgap absorption in the PDS data.

Comparing the light-induced volume expansion and the light-induced PC degradation as well as the defect creation, we found that, firstly, the better electronic stability of the HW a-Si:H does not result in a smaller light-induced volume expansion; secondly, in this group of HW films both the light-induced volume expansion and the light-induced photodegradation decrease when the film deposition temperature increases as shown in Fig. 4 and Fig.5. While, the Fermi-level position and the defect DOS do not monotonically decrease as T_S increases, as shown in Figs. 6 and 7(b).

I.4. Summary and discussion

The hydrogen content, microstructure, and its light-induced metastable changes were studied by IR, DIR and NMR in device-quality a-Si:H samples that were prepared by hot-wire, and glow-discharge CVD with and without H-dilution. Despite the large difference in H content between the HW and the H-diluted PE samples, 1-3 at.% and 8 at.%, the H bonding configuration, its distribution, and the light-induced increase of IR absorption are qualitatively the same. i.e. the predominance of Si-H bonds, ~1/3 of the H in the isolated phase, and an IR absorption increase ~1% near 2000 cm^{-1} upon 90 mW/cm^2 light-soaking for about one hundred hours. In contrast, the non-H-diluted sample with 15 at.% hydrogen contains $Si-H_2$ bonds in addition to Si-H bonds, ~85% H is clustered, and a combination of increase and decrease of the DIR signal is observed. In agreement with previous studies, we find that the Si-H bond configuration and an isolated distribution of Si-H are preferred for more stable materials such as the H-diluted PE and the HW films. The additional metastability is related to the H cluster and/or $Si-H_2$ bonds in the non-diluted PE film, in which the metastable decrease in absorption at ~ 2025 cm^{-1} was found. However, both the mechanism that causes the decrease at ~2025 cm^{-1} and how this relates to DB creation remain unclear.

Interestingly, the NMR results indicate that a 20-80% volume fraction contains nearly no H in all the samples. This implies that there is an inhomogeneity of the backbone amorphous silicon network, in addition to the inhomogeneity of the H distribution. As little as ~0.3 at.% isolated-H atoms are distributed in only a ~20% volume fraction in the HW film, whereas ~2-3 at.% isolated-H atoms are distributed in the majority of the volume (80%) in the PE films. The overall picture is that the PE produces a more homogenous a-Si:H network. The AFM results also indicate a better homogeneity of the PE than the HW films. However, the tightly compacted clusters and the large H-poor volume fractions of ~80% in the HW films indicate improved structural ordering that could contribute to the improvement of electronic stability of the HW films.[2,16,19] More detail will be discussed in section V.

Initial and photo-induced stress were studied in a group of hot-wire a-Si:H films deposited in a wide temperature range, from 280 to 440 ˚C. We observed a photo-induced increase of the compressive stress, that is, a volume expansion on the order of 10^{-5} of the initial value. The change is on the same order of magnitude as that observed in PE films. We found that both the initial compression and the light-induced volume expansion decrease monotonically with decreasing Si-H bond concentration in the HW films.

The density of metastable defects deduced from the PC and the sub-band gap absorption shows a slight difference for most HW films. The largest difference was found for the film deposited at 360 ˚C, in which the AFM (Fig. 7b) shows the highest inhomogeneity. The light-induced defect density was on the order of $10^{16}cm^{-3}$. No simple correlation between the SWE and the light-induced expansion was found in HW films, and none of the PC degradation curves obey a stretched-exponential rule.

Many experimental results have shown that the PC degradation cannot be explained by the bimolecular-recombination model, in which the PC is inversely proportional to the density of D^o. However, two or three types of recombination centers, such as neutral and charged DBs, can explain the experimental results. It is known that the conductivity in intrinsic a-Si:H is dominated by mobile electrons. Therefore, the lack of agreement between the PC degradation and the metastable defect creation can be understood if the film contains charged defects.[1, 33]

Based on the above experimental results, we conclude that the amorphous silicon network is not a near-ideal continuous random network (CRN), but is rather an inhomogeneous network. One possible picture is that the film contains less ordered regions connecting more ordered domains, i.e. a two-amorphous-domain model in the simplest picture. Specifically, the interfacial regions between the phases are likely to be highly disordered and to contain clusters of H occupying shallow Si-H levels. The more ordered phase contains nearly no H (the H absent region found by NMR). Based on experimental observations of light-induced H motion, and H-mediated structural changes in μc-Si:H due to grain boundary motion,[34] it is possible that such hydrogenated interfacial regions are unstable under light-soaking and thermal annealing, due to the catalytic function of locally mobile H in rearranging the local Si network structure. We then describe the creation, saturation and annealing processes of the light-induced metastable changes as follows.

A significant fraction of the energy deposited by carrier recombination may drive the local motion of H atoms, so that the local bonding configurations may fluctuate, leading to fluctuations in the positions of the interfaces. The differential of local order across an interface situated between high- and low-ordered phases will entropically favor its motion into the more ordered phase, corresponding to the growth of the less ordered phase, and the increase in overall structural disorder and entropy. Indeed, the light-induced reversible change of structural ordering in a-Si:H have been reported.[35] Furthermore, the H flipping defects [25] could take place, and provide a significant means for the local motion of the H at the interfaces. However, these mechanisms alone should not create DB defects. Besides the increase in structural disorder, another driving force for structural change is the minimization of lattice strain energy. The tendency of the network to minimize the strain per bond by propagation to the rest of the network causes the growth of the less ordered phase to be imperfect, and leads to the creation of coordination defects (metastable DBs) that occur in conjunction with the phase-growth. This two-phase picture is consistent with the weak-bond breaking model,[21] and suggests a spatial location of the weak bond, i.e. in the vicinity of the interface.

The strain initially concentrated at the interfaces is spread to the rest of the network as the growth of the less ordered phase proceeds, so that the interfaces gradually become less strained and stabilize, eventually leading to the end of the phase-growth process. Under the condition of thermal annealing, the energy is made available to all the atoms, with the help of H-motion [34] the re-growth of the more ordered phase will be favored to satisfy local minimization of atomic configuration energy. This process, obtained by annealing at a suitable temperature, effectively reverses the phase-growth induced by light-soaking, and metastable DBs are annihilated as the strain is reconcentrated at the interfaces and the material approaches a structural state similar to, but not necessarily the same as, the initial state.

The above phenomenological description of the metastability can be reconciled with the experimental results outlined above. The improved electronic stability of the H-diluted PE and the HW films are likely due to the predominance of Si-H (i.e. no SiH_2), and better overall network ordering. Proton NMR finds more clustered H, suggesting more metastable interfaces, in the non-diluted film, and the DIR results suggest that SiH_2 may lead to an extra metastability. The observation that the IR absorption coefficient exhibits metastable changes on the order of 1% is consistent with a picture in which at least a few percent of the H are involved in bonding rearrangements related to the metastable phase growth process. The lack of full recovery of the metastable changes indicates that the annealed structural state is not exactly the same as that of the initial state A, which is suggested by the model described here. The metastable increase in compressive stress would accompany the increase in volume fraction of the less ordered, less dense region, as well as the spreading of the strain initially concentrated at the interfaces to the rest of the network. The HW films are evidently much more inhomogeneous than the PE films, suggesting a larger fraction of interfacial regions in the HW a-Si:H. Thus, even though the HW film has much lower H content, a greater fraction of its H is likely to be associated with the metastable interfacial regions than that of the PE material. This is supported by the NMR observation that the H clusters contain much larger number (>14 atoms) of H atoms in HW a-Si:H than that (6 atoms) in PE a-Si:H. Therefore, given the more inhomogeneous microstructure of the HW film, the model suggests that the magnitude of its light-induced structural changes should be larger than expectations based solely on H content, in agreement

with the LOB and DIR data. Indeed, the photoinduced stress in the HW films only decreases by a factor of 2 over a range of H content that changes by a factor ~ 8.

In summary, the light-induced metastability of a-Si:H contains structural changes in conjunction with the metastable DB creation. We describe the light-induced metastability by a two-phase amorphous model. We emphasize that both the reduced H clusters and the improved overall structure ordering are crucial for the improved stability. Evidently, the high-H-diluted PE-CVD films grown just before the onset of microcrystallinity have shown improved stability as good as the HW film. No unique correlation was observed between the light-induced structural changes and the PC degradation in HW-CVD films. The inhomogeneity of the amorphous silicon network could be crucial to explain the above results.

II. Optical and Electronic Properties of Microcrystalline Silicon as a Function of Microcrystallinity [5-9]

II.1 Introduction

Microcrystalline silicon (μc-Si) is a composition of crystalline grains embedded in an amorphous silicon matrix. The sum of crystalline and grain-boundary (g.b.) volume fractions can be determined by Raman spectroscopy. μc-Si has been used in thin-film device technology, such as contact materials and as an active layer in thin film transistors (TFTs) or in solar cells. The most stable a-Si:H solar cell has been obtained at just before the onset of microcrystallinity as determined by Raman and high-resolution transmission electron microscopy. μc-Si can be directly deposited at low temperatures of 200-300 °C in a PE-CVD system. However, the reaction gas must be highly diluted by hydrogen, for example with R =150, which leads to a very low deposition rate. Many efforts have been made to increase the deposition rate, such as using very high frequency plasma CVD. Nevertheless, a one-step low temperature and high growth rate process is desirable for device applications. Hot wire chemical vapor deposition can achieve a high growth rate with reasonable material quality. By using the HW-CVD technique, a high deposition rate of ~10 Å/s can be reached. However, the typical deposition temperature ~360 ˚C is too high for thin-film-device processes. Therefore, we investigated μc-Si films deposited by HW-CVD at a considerably lower temperature of 240 ˚C. We have studied the Raman and PL spectra from the surface layer on this group of films and explained the features of the low energy PL by a tail-to-tail transition at grain boundaries. We further studied the dependence of the microcrystallinity on film thickness by comparing Raman and PL spectra obtained by front-excitation and back-excitation (with laser beam incident on the film through the transparent substrate) of the film, and by excitation wavelength dependence of the PL spectra. To gain insight into the mechanism of the optical and transport properties, the density of electronic states was studied by optical absorption spectra using the CPM and PDS. We further studied the electron transport properties by conductivity temperature dependence. In this work, the optical and electronic properties as a function of microcrystallinity from onset- to near-saturation were systematically examined.

II.2 Samples and Experimental Conditions

The films were deposited at a substrate temperature of 240 ˚C on Corning 7059 glass. The hydrogen-dilution ratio, R, was varied from 1 to 20 with a gas pressure of 30 mTorr. The sample parameters and the structural characteristics are listed in Table IV. The X-ray diffraction measurements show that the H-dilution threshold for structural transition from amorphous to microcrystalline growth was R=3 and that the average crystallite size was larger than 10 nm. The film thickness decreased from 4.1 to 1.1 μm, and the H content decreased from 13.3 to 3.9 at.%. The film retained the properties of a good photoconductor when R<3. It became less photo-sensitive with the increase of microcrystallinity.

The Raman spectra were measured by using a Spectra-Physics model 2017 Ar^+ laser with a Dilor XY spectrometer equipped with a LN_2-cooled CCD camera. The data were taken at room temperature using the 514.5 nm Ar^+ laser line. The power of the laser was kept below the level which would thermally

induce crystallization. The 514.5 nm and 632.8 nm lines from Ar^+ and HeNe lasers were used with power densities of 30-100 mW/cm^2 for the PL excitation. The samples were mounted on a cold stage which provided a temperature range from 80 to 300 K. The PL spectra were analyzed using a grating monochromator and detected by a LN_2-cooled Ge detector. The optical system was calibrated by a standard lamp. The optical absorption spectra were studied by using CPM, PDS, and transmission spectroscopy (TRS). The x-ray diffraction (XRD) results were supplied by D.L. Williamson.[5,11] We studied several sets of the films with the same R which were deposited during separate runs, and additionally we obtained the spectra from several spots on each film; all the data were reproducible.

Table IV Sample structure and parameters

Sample ID	H_2/SiH_4 (R)	XRD	Grain size L (nm) (111), (220)	Thickness (μm)	Dep. Rate (Å/s)	H content (at.%)	Dark- conductivity (Ohm·cm)	Photo- conductivity (Ohm·cm)
T516	1	a-Si	~ , ~	4.1	17.2	13.3	1.0×10^{-9}	2.0×10^{-5}
T534	2	a-Si	~ , ~	3.0	12.5	10.9	1.6×10^{-9}	7.6×10^{-5}
T532	3	a-Si+μc	10.5, 13.2	1.7	7.08	4.0	4.0×10^{-7}	9.3×10^{-5}
T529	4	μc	7.1, 26.9	2.4	8.0	4.2	1.2×10^{-6}	9.8×10^{-5}
T528	5	μc	10.7, 35.1	2.1	7.0	3.1	5.2×10^{-4}	1.0×10^{-3}
T518	10	μc	18.7, 32.1	1.4	3.9	4.7	2.6×10^{-6}	3.4×10^{-5}
T519	20	μc	28.2, 10.7	1.1	2.3	3.9	1.6×10^{-6}	1.9×10^{-5}

An Ar-ion laser with output power of 0.25 W/cm^2 at 514.5 nm was used for PL excitation. The corresponding absorption depth is 800 Å in an undoped a-Si:H. The emitted photons were dispersed in a monochromator and detected by a liquid-nitrogen-cooled Ge detector through the glass side of the samples. A lock-in technique was used to collect the PL signal. The response curve of the detector and the system optics were calibrated with a linear response detector.

II.3 Results

2.3.1. Raman Spectra from Surface and Interface Layers

The penetration depth of 514.5 nm laser light is 60-200 nm in the case of a-Si:H and μc-Si, respectively. Thus, the Raman measurements probe only a thin surface or interface layer. We show in Fig. 8 the Raman spectra for the group of films listed in Table IV. Fig. 8a shows that the narrow c-Si TO mode at 520 cm^{-1} emerged in the surface layer when R≥3. The relative intensity of the crystalline peak increases with increasing R. The spectrum was decomposed into three components: the crystalline component peaked at 520 cm^{-1}, the amorphous component peaked at 480 cm^{-1}, and an intermediate component peaked between 494-507 cm^{-1} which is associated with bond dilation at grain boundaries. The crystalline and grain boundary volume fractions, X_c, and X_{gb} were estimated from $X_c=(I_c+ I_{gb})/[Ic+I_{gb}+y(L)I_a]$ and $X_{gb}=I_{gb}/[I_c+I_{gb}+y(L)I_a]$, where I_c, I_a, and I_{gb} are integrated intensities of the crystalline, amorphous, and intermediate peaks, respectively, and y is the ratio of the cross section for the amorphous to crystalline phase which varies with the grain size L, where y(L)=0.1+exp[-(L/250)]. Using the L value given by X-ray in Table IV, we found that the crystalline volume fraction X_c increases monotonically from 68% to 92% as the H dilution ratio R is increased from 3 to 20; meanwhile, the g.b. fraction X_{gb} decreases from 48% to 21%. Thus, both the crystalline volume fraction and grain size increase with increasing H-dilution in the surface layer.

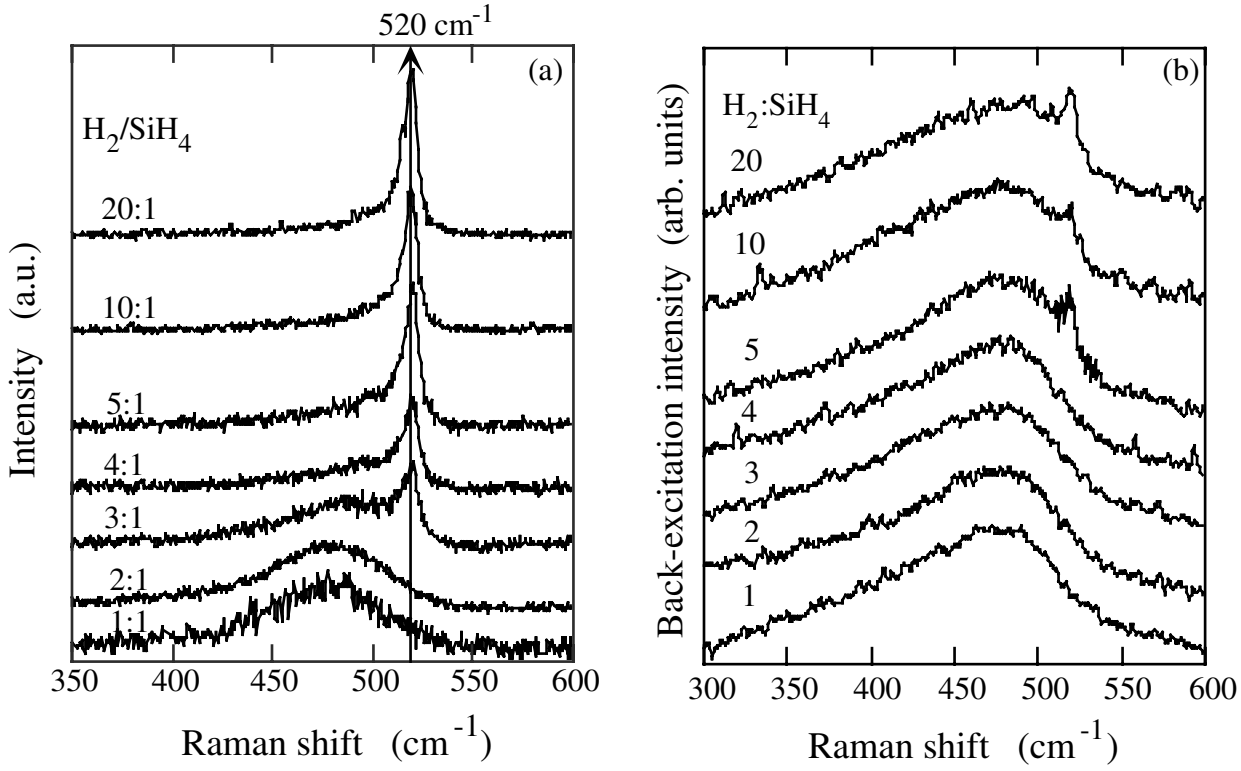

Fig.8 (a) Raman spectra from (a) front- and (b) back-excitation for various H-dilution ratios.

However, the region of interest in TFTs is the 10-20 nm interface layer adjacent to the insulator, whereas in solar cells it is the 100-200 nm layer adjacent to the doped-layer. As we saw in Table IV, all the film thicknesses are greater than 1.0 μm. Therefore, it is important to investigate the dependence of the film properties on thickness. In Fig. 8b, we show the Raman spectra at room temperature for back-excitation of the same group of films described in Table I. The H-dilution ratio, R, is indicated in the figure. All of the spectra were shifted for comparison after subtracting the baseline. One can see that the interface layers are dominated by the amorphous-mode up to R=20. The crystalline-volume fraction is only 2-3% in the interface layers for high-H-diluted films with 5<R<20. The detection of the c-Si Raman-active mode may be limited by both the small number and the small size (< 3 nm) of the crystalline-grain seeds in the interface layers. Interestingly, the band widths of the Raman spectra are about 120 cm^{-1}, which are much broader than those from the surface layer at ~ 70 cm^{-1}. The band width exhibits no change with hydrogen dilution. This implies that the formation of the initial layer is affected by the glass substrate rather than H-dilution. In Fig. 8b, we further compare the Raman spectra from the surface and interface layers in low-(R=1), medium-(R=3), and high-(R=20) hydrogen diluted films. The corresponding film thicknesses are 4.1, 1.7. and 1.1 μm. The thin and thick lines correspond to the Raman spectra obtained by front-surface and back-interface excitation, respectively. For the Raman spectra from the interface, the spectra are fitted with Gaussian peaks at the positions of the three modes of a-Si:H: the longitudinal acoustic (LA) mode centered around 330 cm^{-1}, the longitudinal optic (LO) mode centered around 445 cm^{-1}, and the transverse optic (TO) mode centered around 480 cm^{-1} and the crystalline TO mode near 520 cm^{-1}. Comparing the Raman spectra from the surface to that of the interface layer, one can see the same tendencies in all the films such as the narrowness of the 480 cm^{-1} band, the weakness of the 330 cm^{-1} LA and 445 cm^{-1} LO modes, and the enhancement of the 520 cm^{-1} c-Si mode. These indicate that the structural ordering is improved and the crystalline volume fraction is increased as the film grows thicker for all the H-diluted films in this study.

2.3.2. PL Spectral Lineshape as a Function of Crystallinity

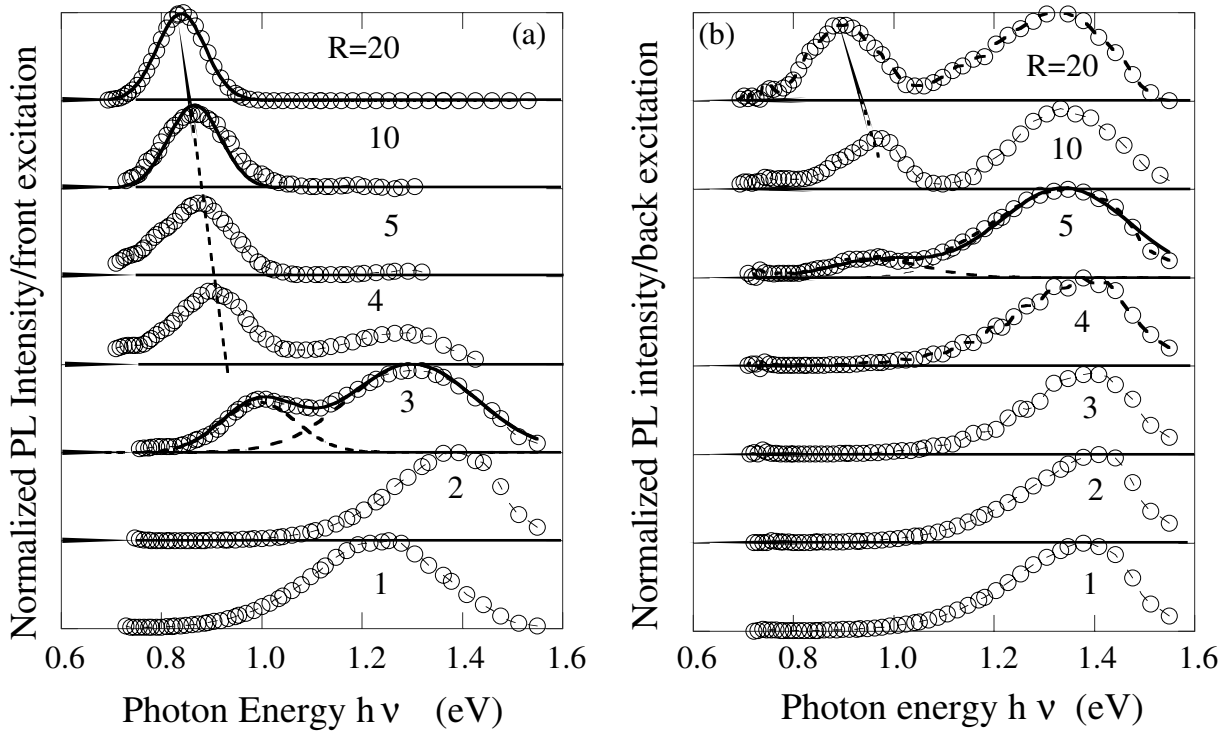

Fig. 9 PL spectra for (a) front- and (b) back excitation with 514.5 nm laser beam for the same films as in Fig. 8.

The normalized PL spectra obtained at 80 K using 514.5 nm excitation are shown in Figs. 9a and 9b. The H-dilution ratio, R, is indicated. Again, with an excitation wavelength of 514.5 nm, the PL spectra reveal only the structure of a 60-200 nm thin layer. PL spectra from the top surface layer are shown in Fig. 9a. In addition to the broad a-Si PL band at ~1.35-1.4 eV, a much narrower band (0.12-0.18 eV) at ~0.9 eV appears when R>3, which is the H dilution ratio where the c-Si 520 cm^{-1} TO mode appears in Raman spectrum as shown in Fig. 1b. As the c-Si volume fraction increases with R, the a-Si luminescence fades away and the low energy PL gradually dominates. This is also consistent with the Raman results (i.e.- the c-Si 520 cm^{-1} TO mode gains intensity gradually with an increase of R). In the interface layer shown in Fig. 9b, the PL from the a-Si phase dominates up to R=5. The top two PL spectra show a dual-peaked feature correlated with the emergence of the c-Si peak in the Raman spectra (see Fig. 1a). It is reasonable to observe the correlation between Raman and PL spectra, since both measurements probe the same layer of the materials by using the same wavelength 514.5 nm laser beam. We see that the PL energy position is quite sensitive to the changes of the microstructure. We have noticed the following interesting behavior of the low energy PL band: (a) the energy peak position shows a red-shift with an increase of H-dilution such as from 1.0 to 0.84 eV when R increased from 3 to 20 as shown in Fig 2a, and (b) the peak energy position is more red-shifted in the surface than in the interface layer. For the films with R=20 and 10, for example, the PL energy peaks at 0.84-0.87 eV and at 0.9-0.96 eV in the surface and the interface layer, respectively. Nevertheless, the low energy 0.84-1.0 eV PL band is related to the emergence of c-Si grains and grain boundaries.

2.3.3. PL Spectra Lineshape as a Function of Film Thickness

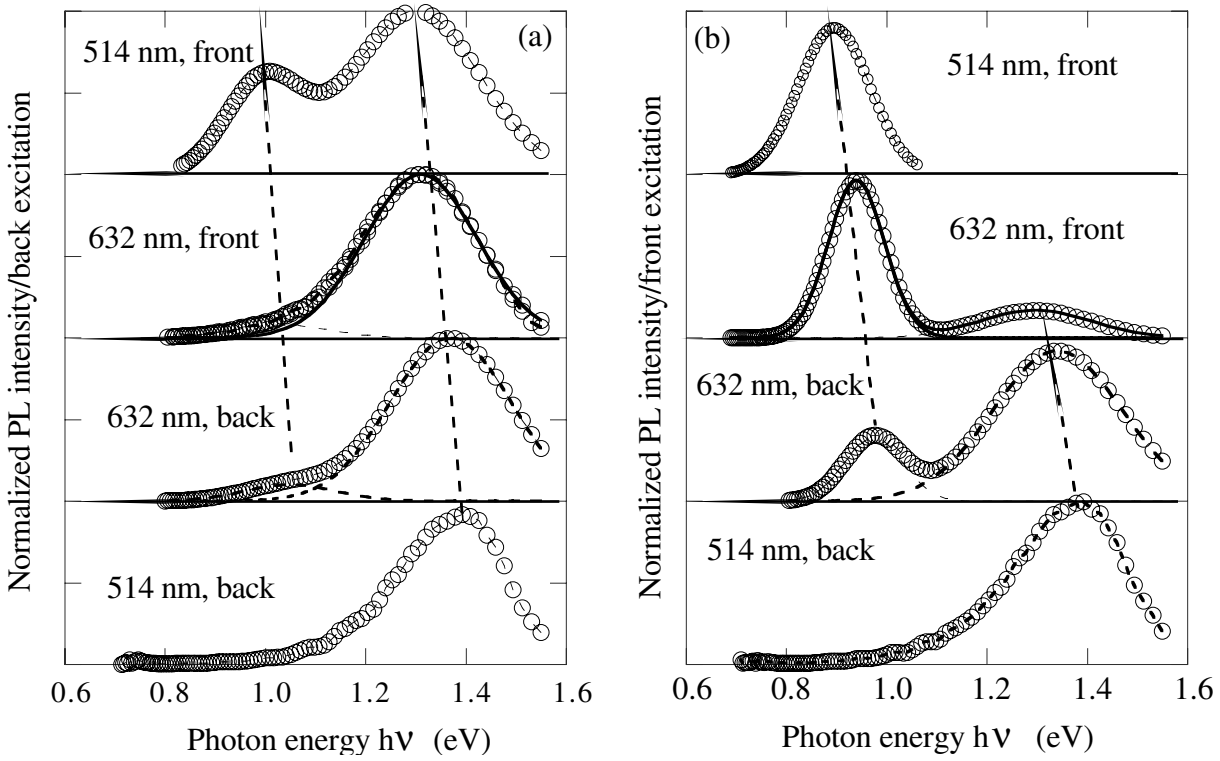

Fig. 10 PL spectra for films with (a) R=3, and (b) R=4 using front- and back excitation with 514.5 nm and 632.8 nm laser lines.

To compare the optical properties in a thin layer to a thicker layer in the same film, we carried out the PL measurement with excitation by a 632.8 nm laser beam where the penetration depth is ~0.3 to ~1 μm in the films, roughly 5 times larger than for the 514.5 nm beam. Figs. 10a and 10b show the results for films with R=3 and 4 using front- and back-excitation with 514.5 and 632.8 nm. In this way, the luminescence behavior has been sampled nearly throughout the film from the interface to the surface layer. Let us examine the results, starting from the interface layer and moving through the surface layer (i.e. from bottom to top curve in Fig.10). As the detected layer moves up closer to the surface, the common features of the PL spectra from these two films are (a) a more pronounced low energy PL band, and (b) a red-shift in the peak energy position for both the high-energy a-Si and the low-energy PL bands. These features result from an increase of crystalline volume fraction and an improvement of structural ordering as the film grows thicker.

2.3.4 Optical Absorption Spectra

To gain insight into the material properties, the density of electronic states was studied by optical absorption spectra. The measurements were carried out by light incident through the top surface of the film. The intrinsic absorption data on the high energy side are deduced from TRS, whereas, CPM gives the low-energy absorption data where the penetration depth is large. Therefore, the absorption coefficient is the average throughout the whole film. Figure 4a shows the optical absorption spectra obtained by using CPM and fit by TRS for this group of μc-Si films. The typical absorption spectra of c-Si and a-Si:H are plotted for reference. One can see that the absorption spectra for μc-Si films are separated into two regimes: (a) when R<3, i.e. before any measurable microcrystallinity appears by Raman, PL and x-ray (see Figs 8, 9), the spectra contain three parts as does the spectrum of a-Si:H. However, an absorption peak at ~1.25 eV appears and is accompanied by a decrease of the intrinsic absorption. (b) When R>3, all

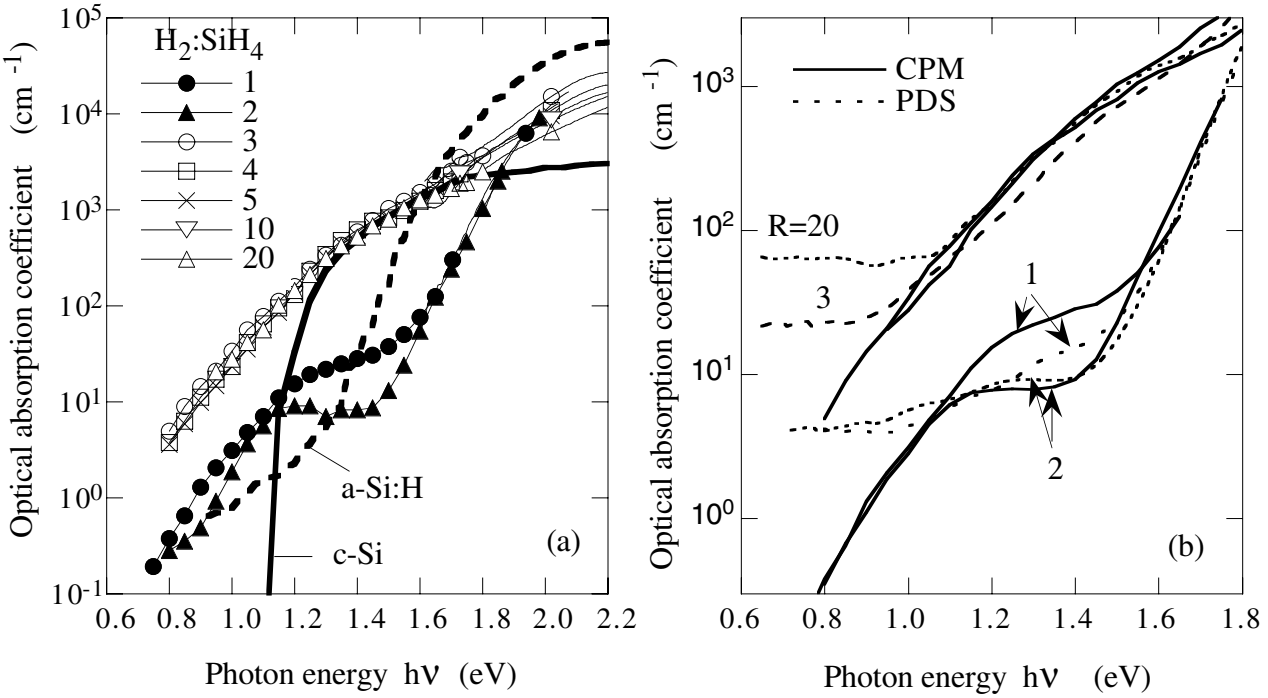

Fig. 11 Optical absorption spectra for μc-Si films with varied microcrystallinity. (a) Spectra obtained by CPM and fit by TRS (the absorption spectra for typical a-Si:H and c-Si are plotted for reference), and (b) comparison of the absorption spectra obtained by PDS and CPM for the films with H-dilution ratios of R=1,2 3, and 20.

the spectra show a similar lineshape, and the absorption coefficient increases about two orders of magnitude when hν <1.3 eV but decreases about one order of magnitude when hν >1.7 eV. When hν < 1.6 eV, there is not much difference of the absorption coefficient between the films with 3<R<20; however, when hν > 1.6 eV one finds a gradual decrease in the absorption with increasing H-dilution. Furthermore, PDS measurements were carried out for the same group of films. The results were consistent with the CPM/TRS data when hν > 1.1 eV, confirming the two regimes of absorption spectra of μc-Si films. In Fig. 4b, we show the CPM and PDS spectra in low-(R=1,2), medium-(R=3), and high-(R=20) hydrogen diluted films. The results are consistent with each other when hν > 1.1 eV, but the PDS gives a much higher absorption when hν < 1.1 eV. The low-energy absorption is shown to be higher for films with higher microcrystallinity. We believe that this is due to the increase of the surface roughness with increasing microcrystallinity. Interestingly, both CPM and PDS show that the 1.25 eV absorption peak of the R=2 film is lower than that of the R=1 film . The other interesting point is that, for the R=1 film, the absorption at 1.25 eV is a factor of two larger by CPM than PDS. Concerning the differences between these two techniques, the CPM would give a larger signal if there were charged states with a small capture rate, and the PDS would give a smaller signal if the density of states is smaller in the surface layer than in the bulk.

In Fig. 12, the optical absorption spectra for R=1 and R=2 films are fit by a Gaussian function peaked at ~1.25 eV with an exponential tail. We argue that the absorption band at ~1.25 eV is not due to the silicon dangling bond (DB) defect states within the gap of a-Si but that this is due to a separate electronic band relevant to the c-Si grains and g.b. This is evident since (a) the energy position is 0.35 eV different from the DB energy of 0.9 eV, (b) the detectable low energy PL intensity at R>3 shows strong temperature dependence which is not the behavior of defect-PL but can be explained by the carrier thermalization in the band-tail states, and (c), if there was such a high density of defect states, the position of the Fermi level should be pinned at ~ 0.35 eV below the conduction band. We will see shortly that this is contrary to the experimental results.

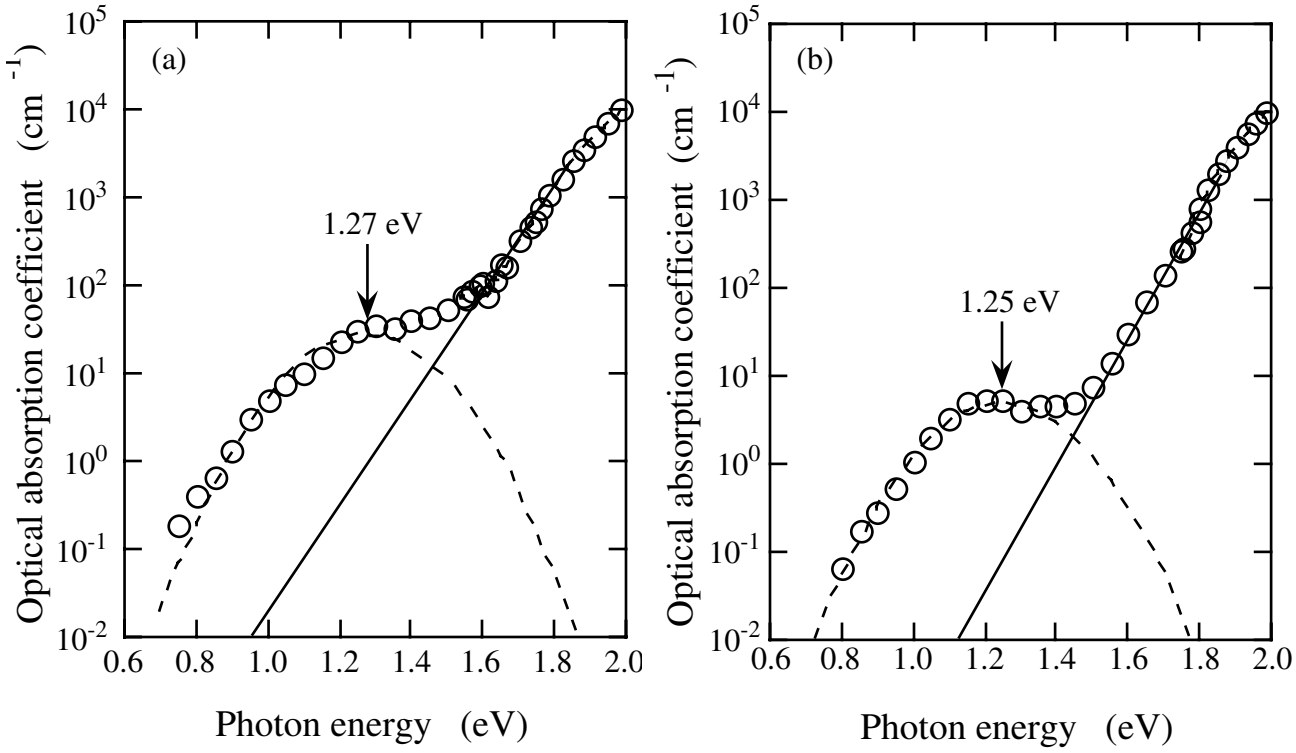

Fig. 12 Optical absorption spectra obtained by CPM and fit by TRS for (a) R=1 and (b) R=2 μc-Si films. An absorption peak appears at ~1.25 eV.

Combining the spectra of photon emission (PL) and absorption, we have a picture of the density of electronic states in these two-phase materials. The density of electronic states consists of two sets of energy bands; one is relevant to the a-Si matrix with an optical gap of ~1.7 eV, and the other sub-band is relevant to the grain/grain-boundary region with an optical gap of 1.2 -1.3 eV. When the carrier diffusion is negligible in transport processes, the carrier transitions will occur between the states within either the a-Si band or the sub-band, but interband transitions will not occur because these two phases are spatially separated. One observes the 1.3-1.4 eV PL band due to the tail-to-tail radiative transitions in the a-Si band, and the tail-to-tail radiative transitions in the sub-band result in the 0.84-1.0 eV PL band. Both the high- and low- energy PL features, such as peak energy position and intensity temperature dependence, can be explained by the thermalization model. At the onset of microcrystallinity (R=1 and 2), the sub-band states are mainly non-radiative states due to the highly disordered Si-Si bond around the small c-Si seeds. This gives the ~1.25 eV absorption peak but no detectable PL. As the bond configuration in the g.b. region improves ($R \geq 3$), these states become radiative, so the low energy PL appears. The two orders of magnitude increase of the absorption coefficient for $h\nu < 1.3$ eV can be understood as the increase in the electronic density of states of the sub-band; the featureless lineshape is due to the energy peak red-shift of both the high- and low-energy PL peaks (see Fig. 10). Integrating over the whole film thickness, one would obtain a broad PL spectra. This is consistent with the broad absorption curve which is an average of all the allowed transitions between the states throughout the whole film.

Since μc-Si is a two-phase material, one can not simply deduce one optical gap from the exponential-like absorption edge. We argue that the absorption spectra originate from two electronic bands. One is the well-known a-Si:H band with an optical gap E_o~1.7 eV; the other band at ~1.25 eV originates from grain boundary related states. Therefore, one could deduce the optical gap for the a-Si phase in the photon energy range of 1.4-2.2 eV according to Tauc plot. Taking an average value from several measurements, we found the largest optical gap of 1.75 eV with the lowest Urbach tail, E_u = 54 meV, for the film with R=2. We will see in the following section that the R=2 film shows the highest photosensitivity.

2.3.5 Conductivity Temperature Dependence and Photosensitivity

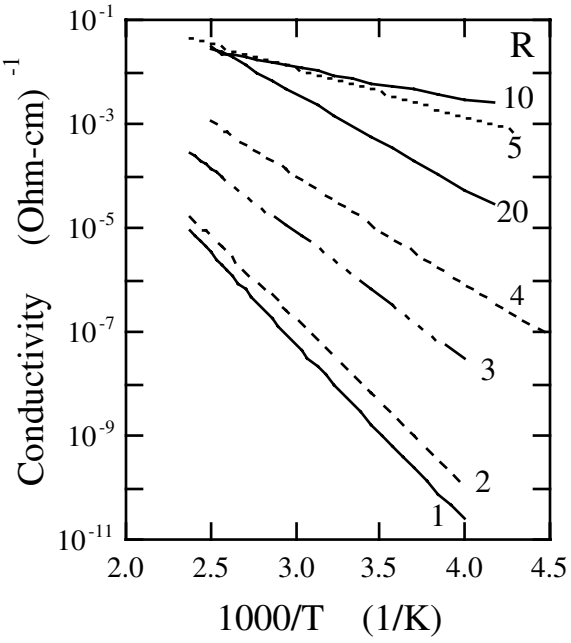

Fig. 13 Conductivity as a function of temperature for the group of μc-Si films with varied H-dilution ratio R.

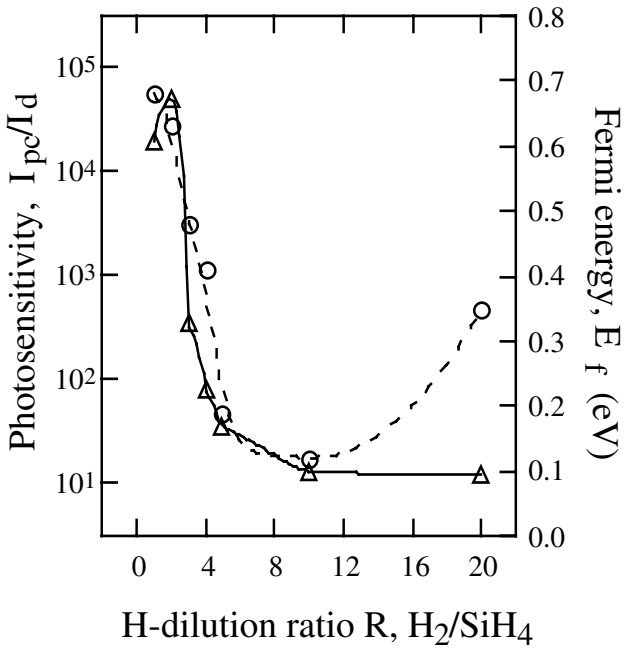

Fig. 14 Position of Fermi-level (○) and the photosensitivity (Δ) as a function of H-dilution ratio R.

Photo- and dark-conductivity are also measured. One set of room temperature results is listed in Table IV. It is clear that the samples have a high ratio of photo- to dark conductivity for R<3. As the film structure changes from a- to μc-phase, the material changes from a high- to low-sensitivity photoconductor. The conductivity curves were obtained by cycling the temperature up and down. The curves were reproducible for the films with R=1,2 and 3. There were non-reproducible data in the increasing-temperature curves for the films with R>3. One possible reason is due to the non-uniformity of the microstructure along the growth direction which causes microvoids to appear between the c-Si grains. However, a thermally activated conductivity of $\sigma=\sigma_o\exp(-E_a/kT)$ was obtained using the decreasing-temperature conductivity curves shown in Fig. 13. We obtain the value of E_a by an exponential fitting. Assuming that electron conduction dominates, the value of the activation energy indicates how much the position of the Fermi level is below the conduction band edge. Fig. 14 shows the Fermi level position, E_f, as a function of H-dilution ratio for this group of μc-Si films. The E_f position moved rapidly from ~0.7 to ~ 0.12 eV (i.e.-from a-Si-like to μc-Si-like) when the film's microstructure transformed from the onset of μc-Si to μc-Si; then, E_f moved down toward the midgap when R=20 with a further increase in microcrystallinity. One can understand this transport mechanism change based on the two-set energy band mode. When R=1 and 2, the electron transport mechanism is a-Si-like, in which electrons move along extended states with an activation energy E_a~0.7 eV. When R≥3 the extended states of the sub-band become dominant in electron transport, and the activation energy changes suddenly from ~0.7 to 0.3 eV and then gradually from 0.3 to 0.12 eV. As the H-dilution increases to R=20, the crystallinity further improves and the transport changes to a crystalline-silicon-like nature. Therefore, the activation energy increases to 0.36 eV. On the other hand, the photosensitivity data (averaged from several measurements) show a maximum at R=2, which is somewhat consistent with the lowest absorption at~1.25 eV. The rapid-transition zone between 3<R<4 for the photosensitivity is the same as that for the transport mechanism.

II.4 Conclusions

In summary, the optical and electronic properties as a function of microcrystallinity in these two-phase materials are listed below:

(a) The electronic density of states consists of two sets of bands corresponding to the a-Si matrix and the c-Si grain/g.b. region. The optical gaps for the a-Si-like band and the sub-band are ~1.7 and ~1.25 eV, respectively.
(b) The onset of microcrystallinity is below the measurement limit of Raman and PL. At this onset, the films are amorphous-like except for the appearance of an optical absorption peak at ~1.25 eV. In this low-microcrystallinity range, there is an optimum condition (R=2 in this study) for solar cell applications for which the film shows the lowest subgap absorption, the highest photosensitivity, and the largest optical gap.
(c) When the c-Si phase is measurable by Raman, a low-energy PL band (0.84-1.0 eV) appears which originates from the tail-to-tail transitions in the sub-band, i.e. the grain boundary (g.b.) regions. The higher ordering of the g.b. structures results in a reduction of the optical gap and, consequently, a red-shift of the PL energy position. Meanwhile, all the absorption spectra show a similar lineshape which is consistent with the overall PL spectra throughout the film.
(d) The conductivity activation energy first decreases from 0.68 to 0.12 eV, then increases to 0.36 eV with increasing microcrystallinity. This indicates the transport mechanism changes from a-Si-like to sub- band-like dominance, and then begins to change to a c-Si-like nature.

III. Electronic Density of States in Transition Materials and Their Solar Cells Studied by PL Spectroscopy [10-14]

III.1. Introduction:

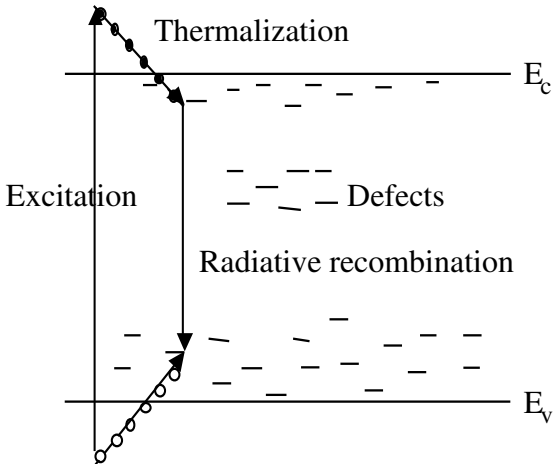

Fig. 15 Schematic diagram of the PL processes.

When non-equilibrium electron-hole pairs are excited by illumination, PL is a measure of the photon emission via radiative recombination centers in semiconductor materials. PL spectroscopy is a sensitive tool not only to characterize the localized electronic DOS but also to find new luminescence centers in a-Si and relevant films. Figure 15 shows the schematic diagram of the processes of PL in amorphous semiconductors. In previous work, it was found that the PL spectrum from intrinsic microcrystalline silicon (μc-Si) could exhibit a dual PL peak at ~1.3-1.4 and ~0.9-1.0 eV. The high-energy band was attributed to the a-Si:H matrix, and the low-energy band emerges when the crystalline volume fraction is relatively large. Hence, the low-energy PL was related to the microcrystallinity. On the other hand, the optical absorption spectra of μc-Si films indicates that the electronic states in the grain boundary (g.b.) region result in an absorption band that peaks at ~1.2 eV; the absorption spectral lineshape changes from a-Si:H-like to poly-Si-like when the film structure changes from a-Si:H to μc-Si. Therefore, the low-energy PL band could originate from the g.b. region. Up to now, the characteristics of this low-energy PL band have not been studied in detail, and the origin of this band remains unclear.

III.2 Characteristics of the Low Energy Photoluminescence in μc-Si Films[9]:

Based on the experimental results from both micro- and poly-crystalline silicon films, there were two typical suggestions for the origin of the low-energy PL. In an early study, it was suggested that the 0.9 eV PL band results from recombination at defect centers in a much more ordered environment. More recently, Savchouk et al. observed PL with a peak at ~0.9 eV in polycrystalline silicon films that contain c-Si grains and grain boundaries. They suggested that the 0.9 eV PL originates from tail-to-tail transitions in boundaries. The exponential tail states in polycrystalline silicon were calculated and examined by Werner et al. using capacitance measurements. μc-Si is a composition of crystalline grains embedded in an amorphous silicon matrix, and the sum volume fractions of crystalline and g.b. deduced by Raman spectroscopy varied from undetectable to >90%. A detailed study of the low-energy PL would give rich information about how the electronic states change with the material structure. Clearly, the origin of the low-energy PL in μc-Si films also needs to be clarified.

In terms of the carrier thermalization in the band tail the temperature dependence of the PL total intensity (I_{PL}) can be described by

$$I_{PL}(T)=I_0\exp[-(T/T_L)] \qquad \text{when } I_{PL}(T)/I_0<<1 \qquad (1)$$

where $T_L= T_0/\ln(\nu_0\tau_r)$ and T_0 is the characteristic temperature of the exponential band tail states $g_0\exp(-E/kT_0)$, $\nu_0=10^{12}$ s^{-1} the attempt-to-escape frequency, τ_r the average radiative recombination lifetime and

I_0 the temperature-independent PL intensity at low T where thermal excitation is negligible. On the other hand, the I_{PL} vs. excitation intensity I_{ex} can be written as

$$I_{PL} \propto I_{ex}^{\gamma} \qquad (2)$$

where $\gamma = 1$ indicates monomolecular recombination such as geminate recombination at low temperature and low excitation intensity; and $\gamma < 1$ for a bimolecular recombination such as nongeminate recombination at high temperature or high excitation intensity. Therefore, the measurements of the PL temperature and the excitation intensity dependence should shed light on the nature of the electronic density of states, i.e. the recombination centers and their recombination mechanism in μc-Si.

We concentrate on the low energy PL peak of the samples in Table VI. The films were deposited at a substrate temperature of 240 ˚C on Corning 7059 glass using hot-wire chemical vapor deposition. The reaction gas was diluted by hydrogen with a ratio $R=H_2/SiH_4$. The crystallinity of μc-Si, X_c, is defined by the volume fraction deduced from the 520 cm^{-1} (c-Si) and ~510 cm^{-1} (grain boundary) Raman mode. The film crystallinity increases with increasing H-dilution ratio. Although both X-ray and Raman measurements show that the structural transition from amorphous to microcrystalline occurred at R=3, the onset of crystallinity as characterized by the optical absorption spectrum was at R=1 and 2. The sample was mounted on a cold stage with a temperature range from 15 to 300 K. PL measurements were performed using either the 514.5 nm (2.41 eV) line of a Ar^+ line or the 632.8 nm (1.96 eV) line of a HeNe laser from the front surface. The PL spectra were analyzed using a grating monochromator and detected by a LN_2-cooled Ge detector. The lock-in technique was used with a light chopper at a frequency of 17 Hz. The optical system was calibrated by a standard lamp. Neutral density filters were used to vary the excitation intensity.

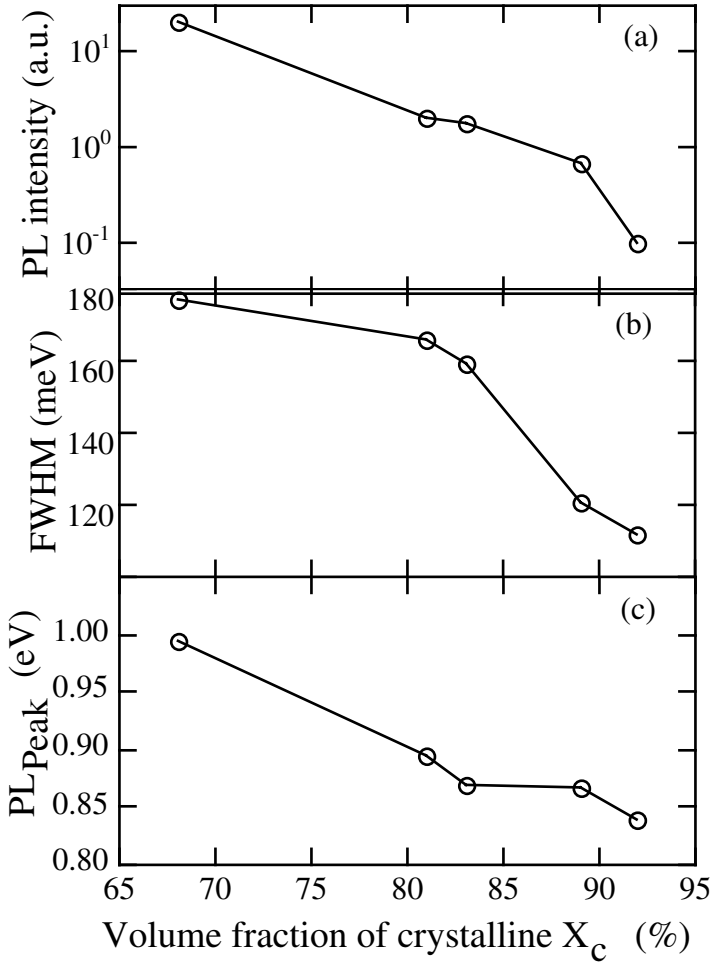

Fig. 16 The low-energy PL at 80 K (a) total intensity, (b) peak energy position, and (c) band width FWHM, as a function of material crystallinity.

We investigated the characteristics of the PL in a group of μc-Si films with varied crystallinity. The typical PL main band that peaked at 1.4 eV in a-Si:H was observed in samples T516 and T534 at 80 K. When the crystallinity X_c was increased to 68% in sample T532, the PL spectrum showed a dual peak at 1.3 and 0.9 eV. As the crystallinity was further increased, the low-energy PL band dominated. We concentrate on the low-energy PL in what follows. Fig. 16 shows the low-energy PL intensity, peak energy position, and FWHM as a function of X_c at 80 K. One can see that as the film crystallinity increases, the interesting features are: (a) the PL intensity decreases by about two orders of magnitude; (b) the band width decreases from 0.18 to 0.12 eV, and (c) the PL peak energy redshifts from 1.0 to 0.84 eV. All of these features imply changes in the recombination centers due to the increase of crystallinity, which induce a decrease in the transition probability and a narrowing of the binding energy distribution. We emphasize that the low-energy PL bandwidth is two times narrower in μc-Si than that in a-Si:H. i.e. FWHM ~ 0.15 eV compared to 0.3 eV.

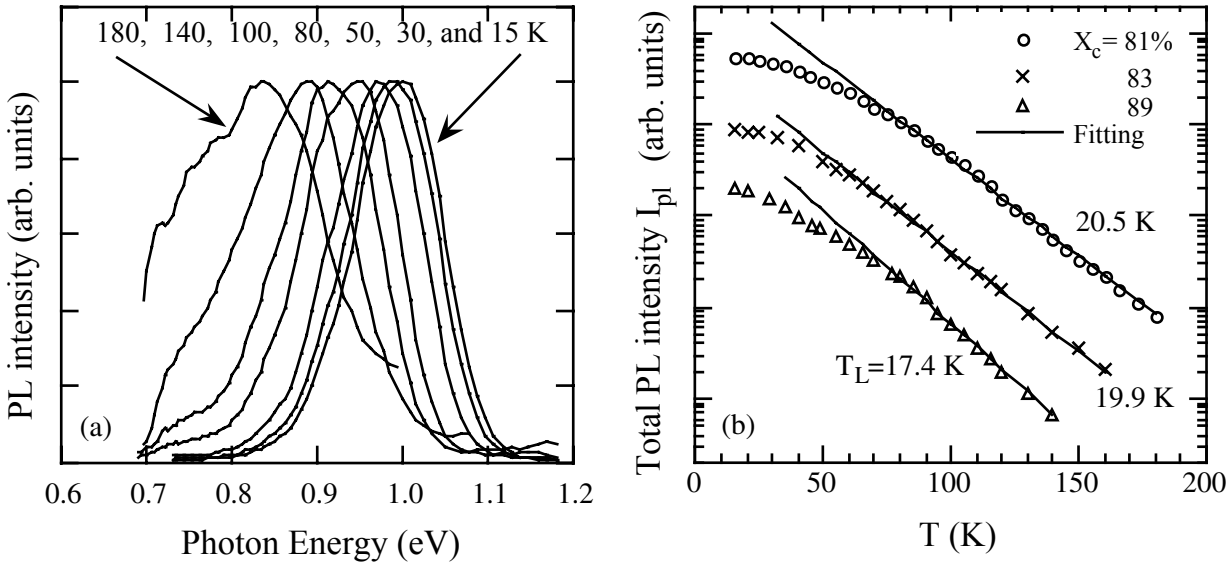

Fig. 17 (a) Temperature dependence of PL spectra for the film X_c=81% using 632.8 nm excitation; (b) Plots of I_{PL} vs T for the films of X_c=81, 83 and 89%, respectively. The solid lines are fit to the data based on Eq. (1).

We further studied the PL temperature and excitation intensity dependence. Fig. 17a shows the typical PL spectra temperature dependence. The spectra were taken of a film with X_c=81% using 632.8 nm excitation. Similar features have been found in other μc-Si films using either 514.5 or 632.8 nm excitations. One finds that the peak energy redshifts by about 170 meV from 15 to 180 K. According to the carrier thermalization model, the PL peak energy reflects the carrier distribution dominated by multiple trapping processes, and the PL peak energy shift follows $E_{peak}(T)-E_{peak}(0)=-E_D$ where $E_D=kT\ln(\nu_0\tau_r)$ is the demarcation energy. Using a reasonable value of the recombination lifetime, $\tau_r \approx 10^{-6}$s for μc-Si, one obtains E_D(180 K)-E_D(15 K) = 180 meV. Fig. 17b plots the total PL intensity $I_{PL}(T)$ vs. temperature for samples with X_c= 81, 83, and 89%. One can see a weak temperature dependence of the PL intensity below 60 K which is characteristic of PL in a-Si:H. This has been explained as resulting from the non-radiative Auger processes at low temperatures. Above 60 K, the PL intensity is rapidly quenched with increasing temperature. The data can be well fit using Eq. (1). We obtain T_L equal to 20.5, 19.9 and 17.4 K for the samples with X_c=81, 86 and 89%, respectively. It is clear that T_L decreases with increasing crystallinity. This is consistent with the observation of the decrease in PL bandwidth with

increasing crystallinity as shown in Fig.16(b). Using the recombination lifetime $\tau_r \approx 10^{-6}$ s, one obtains the characteristic temperature of the exponential tail states, T_0, equal to 283, 275, and 240 K. The value is about two times smaller than that of 500 K in a-Si:H. Again, it is in agreement with the narrower PL bandwidth of μc-Si compare with a-Si:H.

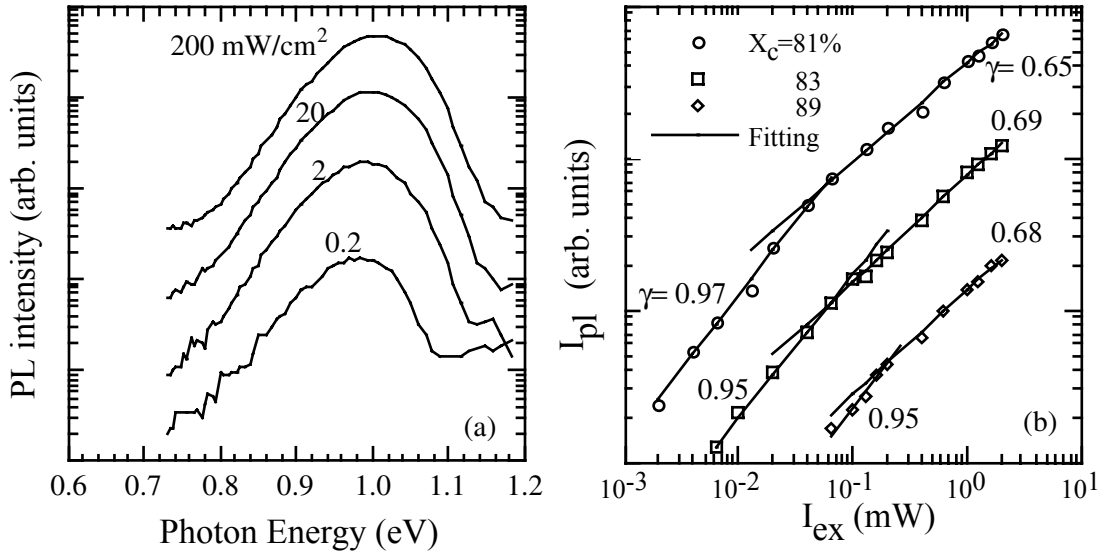

Fig. 18 (a) Excitation intensity dependence of PL spectra at 15 K for the film X_c=81% using 632.8 nm excitation; (b) Excitation intensity (I_{ex}) dependence of the PL integrated intensity (I_{PL}) for the film of X_c=81, 83 and 89%. The open symbols are experimental data. The solid lines are fitted to the data based on Eq. (2).

Fig.18a shows the PL energy spectra as a function of excitation intensity of sample T529. The data were obtained by using 632.8 nm laser excitation at 15 K. One can see that the PL peak shifts to high energy as the excitation intensity increases. This is simply due to the shift of the quasi-Fermi level position toward the band edge with increasing excitation intensity. The total intensity, I_{PL}, as a function of the excitation intensity, I_{ex}, for samples T529, T528 and T518 is shown in Fig. 18b. It is obvious that the excitation intensity dependence shows two regimes. For high excitation intensity (≥ 6 mW/cm^2), we found a sublinear relationship of $I_{PL} \propto I_{ex}^{\gamma}$ with an exponent of $\gamma \approx 0.65$, whereas, there is an approximately linear dependence for low excitation intensity (< 6 mW/cm^2). In general, at low temperature and low excitation intensity the carriers geminately recombine. Recombination becomes non-geminate when the electron-hole pair density exceeds about 2×10^{18} cm^{-3}. This change of mechanism is attributed to the overlap of adjacent pairs.

In summary, we studied PL in μc-Si, which is a two-phase material characterized by crystalline grains embedded in an amorphous matrix. In addition to the typical 0.3 eV broad PL main band from the residual a-Si:H phase, a ~ 0.15 eV wide band at ~0.9 eV has been observed in μc-Si films. Since there is a 1.25 eV optical absorption band originating from the states in the g.b. region in the μc-Si samples, it is reasonable to attribute this low -energy luminescence to the same electronic states. We found that both the total intensity and the lineshape of the low-energy PL are sensitive to the film microcrystallinity. We explain this as follows: when there is no detectable 520 cm^{-1} Raman mode, the grain size must be <3 nm. With such small c-Si grains scattered in the a-Si matrix, the distortion of the bond length and bond angle

in the grain boundary (g.b.) region would be relatively large. Consequently, the relevant electronic states are mainly non-radiative states. Therefore, although there is an optical absorption band at 1.25 eV, no low-energy PL band was observed in samples T516 and T534. The ordering of the structure at the g.b. improves as the film crystallinity increases, and then more electronic states behave as radiative recombination centers. Consequently, the low-energy PL band is observed. With further increase in the crystallinity, the gain size increases and the volume of g.b. decreases. In addition, the momentum conservation in crystalline material reduces the transition probability and a tetrahedral Si-Si bond results in a smaller band gap. This results in a decrease of the PL intensity and a red-shift of the PL peak energy. Furthermore, we found that the PL intensity rapidly quenched with increasing temperature, and there were two regimes of dependence of PL intensity on excitation intensity. All the results can be explained in terms of the carrier thermalization model in an exponential band tail. The PL "tail width" (it could be the occupation of the tail states) kT_0 was found to be 20-24 meV, which is about two times narrower than that in typical a-Si:H. We attribute the low-energy PL band to radiative tail-to-tail transitions in grain boundary regions, so that the defect recombination model for the low-energy PL in μc-Si should be ruled out.

III.3 DOS of Intrinsic Layers in Solar Cells Near a-to μc-Si Transition Studied by PL Spectroscopy:

3.3.1. Sample and Experimental:

Thin film n-i-p solar cells were prepared using decomposition of disilane-hydrogen mixtures by plasma-enhanced chemical vapor deposition. By increasing either the H dilution ratio or the thickness, the i-layer structure showed a transition from amorphous to microcrystalline silicon characterized by x-ray diffraction. The electronic states of the i-layer were examined by PL spectroscopy, which showed that: (a) below the onset of microcrystallinity, a blueshift of the 1.4 eV PL peak energy along with a decrease of the "band width" occur as the structural order is improved; (b) above the onset of microcrystallinity, the PL efficiency decreases by a factor of 4-5 and the PL peak energy is redshifted toward 1.2 eV as the μc-Si volume fraction is increased. In addition, the solar cell open circuit voltage shows first an increase and then a decrease, correlating with the PL peak energy position. We conclude that the PL spectroscopy is a sensitive tool for characterizing the gradual amorphous-to-microcrystalline structural transition in thin film solar cells.

The n-i-p solar cells were fabricated by PECVD on stainless steel substrates. The reaction gas of disilane was diluted by hydrogen. Three dilution ratios, R =1.0, 1.2 and 1.6 were used, where R=1.0 is the standard hydrogen dilution ratio, and R=1.2 and 1.6 represent 20% and 60% more hydrogen dilution, respectively. The i-layer thicknesses were d ≈ 110, 220, and 450 nm. The same sample was used to conduct XRD, PL, and V_{oc} measurements. Relevant cell deposition parameters, XRD results, and V_{oc} are listed in Table V. For PL measurements, the sample was mounted on a cold stage. PL was excited by using a 100 mW/cm^2 632.8 nm laser beam. The absorption depth of the 632.8 nm light in both a-Si:H and μc-Si is greater than the cell thickness, so that average properties of the bulk material are obtained. The PL spectra were analyzed using a grating monochromator equipped with a liquid nitrogen-cooled Ge detector.

Among the nine i-layer materials studied, four of them show c-Si peaks in the XRD data as listed in Table V. The microcrystalline volume fraction is estimated as the ratio of the sum of the (111), (220), and (311) peak areas to the total (a + μc) peak area. It is clear that the μc-Si volume fraction increases as the hydrogen dilution and i-layer thickness increases. Meanwhile, the full-width-at-half-maximum (FWHM) of the first a-Si:H peak tends to decrease with increasing H dilution and with increasing thickness for R=1.0 and 1.6. This effect has been associated with improved medium-range order in a-Si:H. There is a clear correlation between the microcrystallinity and V_{oc}. In Table V, high V_{oc}'s (> 0.95 V) were found for all cells that were detected to be fully amorphous, but low V_{oc}'s (< 0.9 eV) were found for all cells with the μc-Si component. In the cells with R=1.6, one can see that the V_{oc}

monotonically decreases from 0.709 V to 0.466 V when the μc-Si volume fraction increases from ~ 5 % to 36 %. However, XRD and Raman may lack the sensitivity to distinguish changes in the material properties in the cells below the onset of microcrystallinity such as the five cells with R=1 and 1.2, particularly for the thinner i-layers which lead to the rather large experimental uncertainties in FWHM listed in Table V. A more sensitive technique is desirable. More recently, a 1.0-1.2 eV PL band was found to be a characteristic feature of μc-Si from a series of hot-wire CVD transition films. Since the properties of the electronic states are crucial for solar cell performance, we study these transition materials by using PL spectroscopy.

Table V. Characteristics of solar cells and their corresponding i-layers prepared with different H dilution ratios (R), thicknesses (d) and their PL peak energy position at 80 K.

Cell No.	R	d (nm)	FWHM (degrees)	μc fraction (%) (from XRD)	V_{oc} (V)	PLpeak at 80 K (eV)
583	1.0	130	6.4(±0.6)	0	0.962	1.360
591	1.0	220	5.3(±0.3)	0	0.963	1.390
569	1.0	450	5.43(±0.15)	0	0.984	1.420
592	1.2	105	5.1	0	0.955	1.409
600	1.2	215	5.8	0	0.973	1.426
576	1.2	410	4.98	4	0.860	1.400
593	1.6	110	4.5	~ 5	0.724	1.377
579	1.6	220	4.1	27	0.529	1.300
580	1.6	450	3.20	36	0.466	1.273

3.3.2. PL spectra at 80 K

We discuss the PL results at 80 K for the cells below and above the transition, from fully amorphous to partially microcrystalline in Figs. 19(a) and 19(b), respectively. The PL intensity is similar to typical a-Si:H cells in the five cells before the onset of microcrystallinity; their normalized PL spectra are shown in Fig. 19(a). One can see that the PL lineshape shows the effects of both hydrogen dilution and thickness, although the samples did not show any detectable c-Si signal by XRD. Let us first examine the three spectra in the bottom of Fig. 19(a). For the solar cells with R=1.0, when d is increased from 110 to 220 and 450 nm, the PL peak energy is blue shifted from 1.36 to 1.39 and 1.42 eV. At the same time, there is an enhancement of the low energy shoulder (~1.2 eV). The thickness effect is more clearly shown for the two cells with R=1.2, i.e. the two spectra at the top of Fig. 19(a), in that the FWHM of the PL main-band decreased from 0.3 eV to 0.2 eV. On the other hand, for the cells with μc-Si volume fractions from 4 to 36% characterized by XRD, the PL main features are: (a) the total PL intensity decreases by a factor of 4-5 compared to a-Si:H cells because of the decrease of the radiative recombination from the a-Si:H matrix; and (b) there is no longer a blue shift of the PL peak energy because of the relatively large intensity of the 1.2 eV band as shown in Fig. 19(b). It is noteworthy in the top curves of Fig. 19(b) that the 1.2 eV PL band dominates in the cells with μc-Si volume fraction of 27-36%.

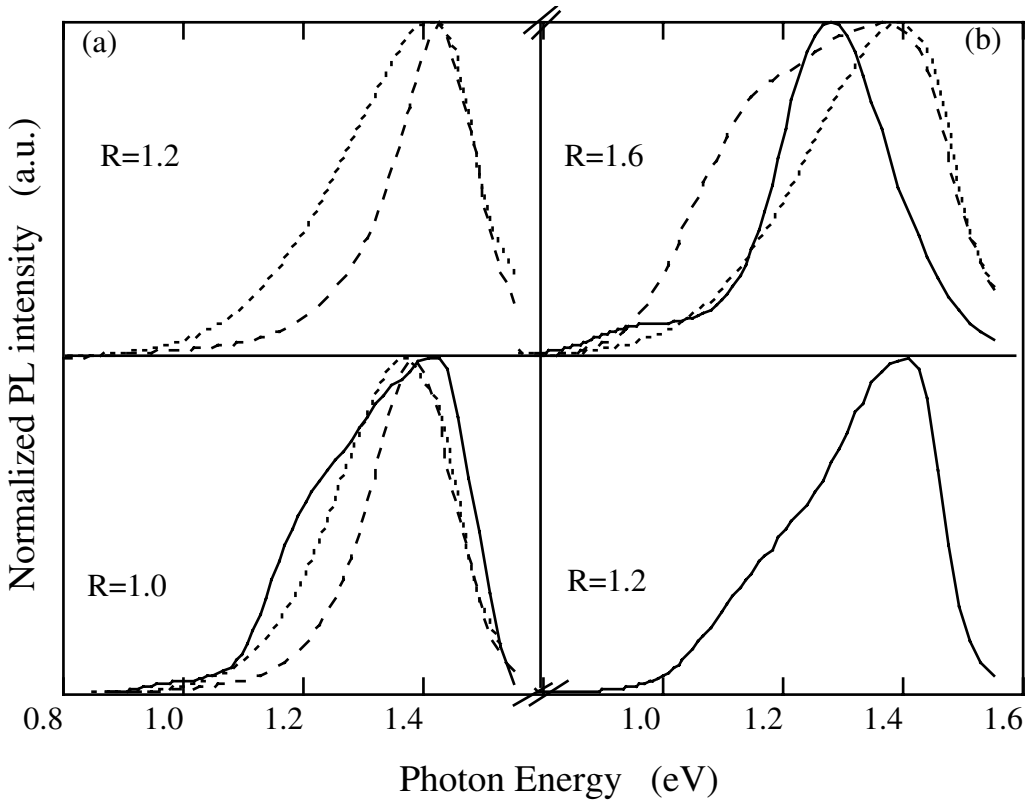

Fig. 19 Normalized PL spectra at 80 K for (a) five cells that are below XRD-detectable microcrystallinity, and (b) four cells that are above the XRD-detectable transition to mixed a-Si:H/μc-Si. The dotted, dashed, and solid lines correspond to sample thickness d≈110, 220, and 450 nm, respectively.

We explain the above observations as follows. First, the increased hydrogen dilution results in an improvement of the medium-range order of the amorphous network. We believe that this results in a narrowing of the valence band tail and then a PL blueshift along with a decrease of the bandwidth. The network order is also improved when the i-layer grows thicker. Second, we believe that a small percentage of crystalline silicon grains, perhaps with small sizes, have gradually emerged in the a-Si:H matrix when increasing either hydrogen dilution or the film thickness. This is indicated by the enhancement of the 1.2 eV PL shoulder in the a-Si:H cells as shown in Fig. 1(a). When the crystalline grains become measurable by XRD, the PL peak energy is red shifted because of the enhancement and finally dominant by the 1.2 eV PL band in the μc-Si cells.

3.3.3. Temperature Dependence of the Low Energy PL

To explore the nature of the 1.2 eV low energy PL bands, we study the temperature dependence of the PL spectra. In Figure 20, we plot a typical group of PL spectra at 200 K from cells of d~220 nm with R=1.0, 1.2 and 1.6. All the three PL spectral lineshapes are completely different from that of typical a-Si:H samples at 200 K. A notable feature is that the relatively large intensity of the 1.2 eV PL band finally becomes dominant in the R=1.6 cell. The other interesting feature is that the 0.9 eV band is also relatively large in the R=1.0 and 1.2 cells. We believe that both features originate from the enhanced radiative recombination in the c-Si grain boundary regions. However, all these spectra consist of three components and can be fit with Gaussian functions peaked at ~0.9 eV, ~1.06-1.2 eV, and ~1.33-1.4 eV. The integral of the PL intensity (I_{PL}) was studied as a function of temperature. According to the carrier thermalization model, I_{PL} vs. T follows $I_{PL}=I_0\exp(-T/T_0)$, where $T_0=T_L/\ln(\nu\tau)$ and T_L is the

characteristic temperature of the exponentially distributed band tail states, ν is the escape attempt frequency, and τ is the carrier recombination lifetime. T_0~23 K has been observed in a-Si:H films and a reasonable characteristic temperature of T_L ~ 480 K was obtained by using $\nu=10^{12}$/s and $\tau\sim10^{-3}$ s. In a recent work, we have suggested that an electronic sub-band is formed from the grain boundary region and the 1.2 eV PL originates from the tail-to-tail transition in that region of μc-Si films. So we expect that the temperature dependence of the 1.2 eV band also follows $I_{PL}=I_0\exp(-T/T_0)$. We plot a group of typical curves in Fig. 21. The solid lines in Fig. 21 are least-square fits yielding T_0 = 21 and 34 K from the 1.4 and 1.2 eV PL, respectively. The former is compatible with the observed value of 23 K in a-Si:H films, the latter is attributed to the tail-to-tail transitions in the grain boundary regions. It is clear that the temperature dependence of the 1.2 eV band is weaker than that of the ~1.4 eV band. The dashed line and diamond symbols in Fig. 21 represent the data from the 0.9 eV defect band of cell #600. The weak temperature dependence is similar to that in typical a-Si:H films. It is worthwhile to mention here that the relatively strong 0.9 eV PL band in the films just before the onset of microcrystallinity does not mean a high defect density. It indicates more radiative transition via dangling bond states in these films than that in non-hydrogen diluted a-Si:H films.

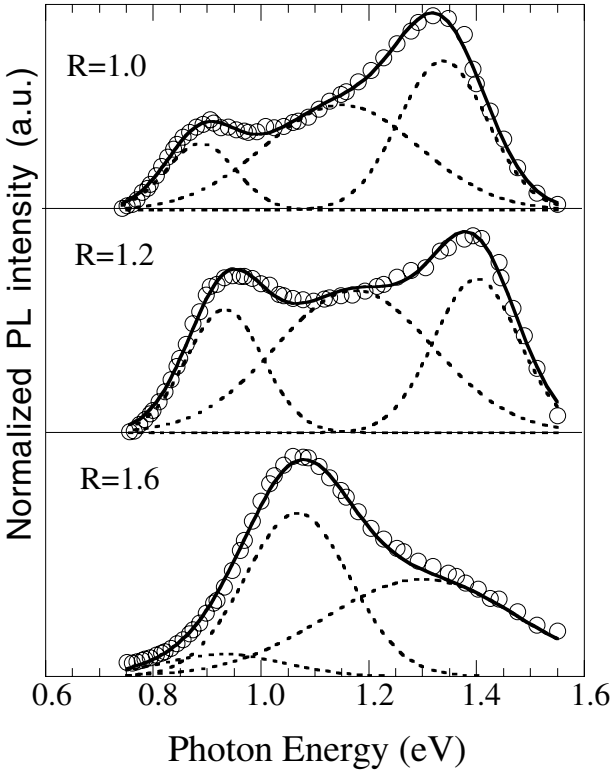

Fig. 20
Normalized PL spectra at 200 K for cells #591, #600, and #579 with d≈220 nm and R=1.0, 1.2 and 1.6. Open circles represent experimental data. Dotted lines are Gaussian functions with their superpositions indicated by the solid lines.

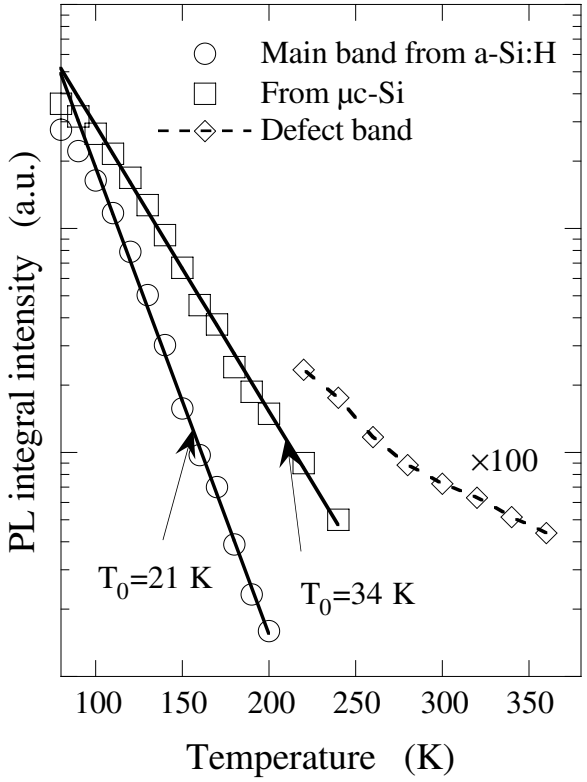

Fig. 21
Integrated PL intensity (I_{PL}) vs. temperature. Open circles and squares correspond to the experimental data of ~1.4, ~1.2 eV bands from cell #579, and diamonds correspond to the data of 0.9 eV PL bands from cell #600. Solid lines are the fits based on $I_{PL}=I_0\exp[\ T/T_0]$.

3.3.4. V_{oc} as a function of the characteristics of PL

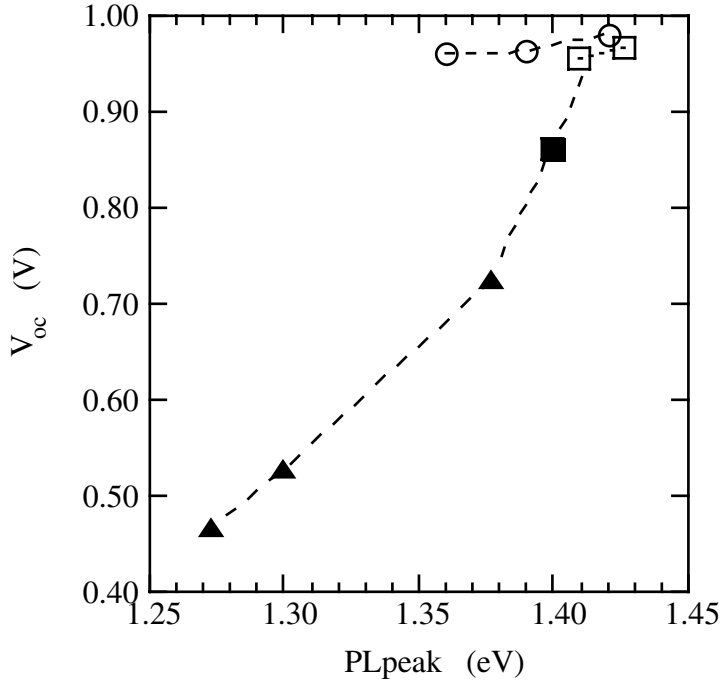

Fig. 22 V_{oc} as a function of the PL peak energy position for the nine near-transition solar cells studied. The open circles and squares represent the five amorphous cells shown in Fig. 1(a). In this regime, V_{oc} increases as the PL is blue shifted. The solid symbols represent the four cells shown in Fig. 1(b). In this regime, the V_{oc} rapidly decreases as the PL is red shifted due to microcrystallinity in the mixed-phase cells.

III.4 Conclusions

In summary, we conclude that the PL spectroscopy is a sensitive tool to characterize the gradual amorphous to μc-Si structural transition in real solar cell configurations. We have shown that the electronic density of states is significantly changed with both hydrogen dilution ratio and the film thickness in these transition devices. The features of the PL spectra and their temperature dependences characterize the gradual improvement of the a-Si:H network order and the transition to μc-Si. Distinguished by the onset of microcrystallinity characterized by XRD, we found that there are two regimes of the PL features for the nine solar cells near transition as shown in Fig. 22. In the five cells below the onset of detectable microcrystallinity, the dominant factor of increase hydrogen dilution and thickness is to improve the a-Si:H structural order. As a result, the PL peak energy is blue shifted and the linewidth is narrowed. In the four cells above the onset of microcrystallinity, the main factor is an increase of the μc-Si volume fraction, which results in the decrease of the total PL intensity and the increase of the 1.2 eV PL band. Meanwhile, the V_{oc} quickly decreases as the PL energy is red shifted and the total intensity decreased. The later is due to increase of density of defects. So, recombination loss also plays a role in the decrease of V_{oc}. Proper conditions such as a combination of hydrogen dilution ratio and thickness at R=1.0, d=0.2-0.4 μm and R=1.2, d=0.2 μm have produced the highest V_{oc} as shown in Fig. 22 and Table V. These are consistent with the most stable high-performance a-Si:H solar cells prepared just before the onset of microcrystallinity.

IV EL and PL spectra From a-Si and a-SiGe p-i-n Solar Cells [15]

IV.1. Introduction:

EL combined with PL has been used to study the density of localized states in a-Si:H base solar cells. Significant differences in the features of the EL and PL were observed. Generally, at low temperature (such as 80 K), the EL peak energy, EL_{peak}, is ~0.2 eV less than that of the PL_{peak}, and the EL efficiency is two or three orders of magnitude less than the PL if the forward current density is used as the generation rate. Spear et al. argued that the EL peak energy was modulated by interference fringes, and the low EL efficiency is due to the EL generated only near the p^+ contact. The above unique EL features have been explained by our model of dispersive-transport-controlled recombination.. In our model, the EL_{peak} is determined by the carrier-transport level rather than the demarcation level determined by carrier thermalization; and the EL generation rate must be the recombination current rather than the forward current which accounts for a gain by factor of 100-1000. The previous studies suggested that the EL spectroscopy gives important information of both the localized states and the carrier transport of p-i-n cells.

In this work, we studied a series of hydrogen diluted a-Si:H cells and a-SiGe p-i-n cells with a varied Ge content. Hydrogen dilution of reaction gas during film growth has been used to improve solar cell performance; and the SiGe alloy has been used as the i-layer in the narrow-gap cells. To understand the device/material physics, one needs to know the density of localized states in the intrinsic layer. Therefore, a comparison study of EL and PL spectra in a temperature range of 80~200K were carried out.

VI.2.Sample and Experimental:

The experimental layout is shown in Fig. 23. It is similar to the PL system except that the excitation source was a pulse generator and an oscilloscope was used to monitor the output.

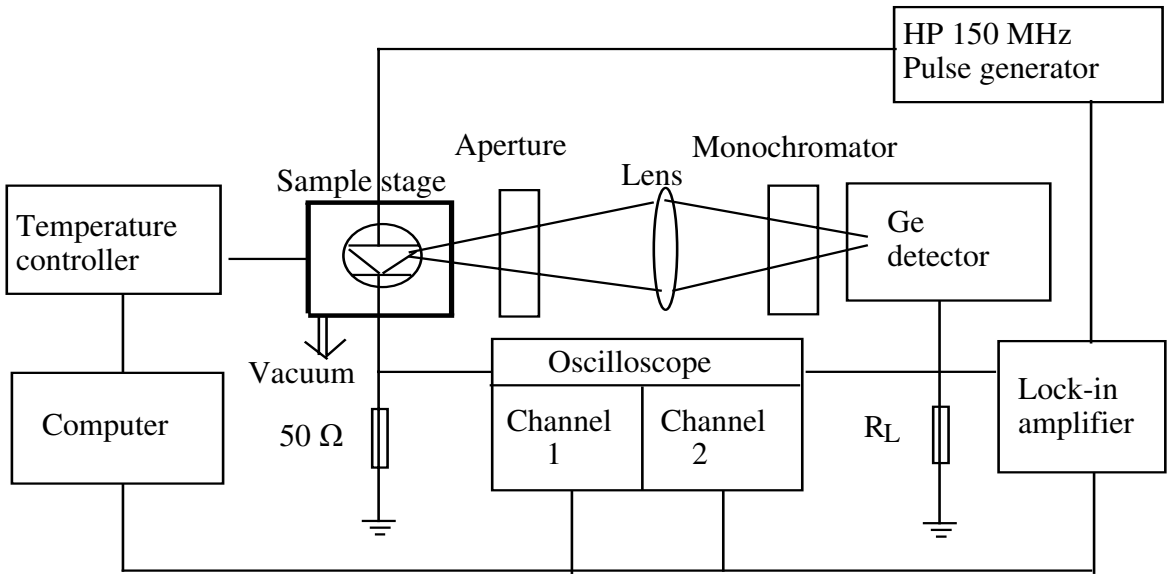

Fig. 23 EL Experimental Layout

Device quality a-Si:H and a-SiGe p-i-n solar cells were prepared by PE-CVD on stainless steel (ss) substrates and on glass substrates. Disilane and/or Si_2H_6:GeH_4 mixture were used for deposition on ss substrates. The i-layer thickness was ~0.2 μm for a-Si:H solar cells and ~0.5 μm for a-SiGe solar cells. The top contact area was ~0.2 cm^2. For EL, a voltage of 5 V was supplied by a pulse generator. The forward bias current density was in the range of 50 to 500 mA/cm^2 in the temperature range from 80 to 200 K. We used a 632.8 nm laser excitation for PL. The penetration depth of the 632.8 nm light in a-Si:H was ~1 μm which is greater than the sample thickness. A bandpass filter at 632.8 nm was used to avoid the IR component of the HeNe laser. The incident laser power was 2 mW. For a-SiGe cells, 514.5 nm Ar^+ laser excitation was used, the incident laser power was 6 mW.

The preparation conditions and the cell performances for H-diluted cells made at the Univ. of Toledo are listed in Table VI. Four groups of cells deposited at 150, 175, 200, and 250 °C were studied. We will pay special attention to the H-dilution effect on V_{oc}. We note that V_{oc} is greater than 0.9 V in all the cells and it increases with increasing H dilution. For the same H dilution, on the other hand, V_{oc} increases with decreasing deposition temperature, T_S. Another group of samples made at BPSOLAR and the Univ. of Toledo are listed in Table VII.

Table VI. Deposition conditions and cell performances for the H-diluted a-Si:H cells

Sample	Substrate temperature T_S (°C)	H_2:Si_2H_6, R	i-layer thickness (nm)	V_{oc} (V)	J_{sc} (mA/cm^2)	FF (%)
GD288	250	20	207	0.931	11.2	71.1
GD290	250	25	215	0.926	10.3	66.2
GD299	250	50	172	0.95	9.7	71.6
GD300	250	100	170	0.948	7.4	66.3
GD289	200	25	186	0.936	9.1	72.1
GD291	200	33	189	0.944	8.9	73.0
GD292	200	50	195	0.951	9.1	71.8
GD298	200	100	153	0.971	8.1	70.3
GD293	175	33	201	0.948	8.9	73.3
GD304	175	50	156	0.985	9.7	71.1
GD294	175	100	160	0.966	6.8	71.3
GD295	150	100	159	0.972	6.4	69.6

Table VII. The PL and EL peak energy and the V_{oc} of a-SiGe solar cells

Sample ID	GeH_4/Si_2H_6	V_{oc} (V)	PLpeak (eV) (at 80 K)	ELpeak (eV)
Group I(UT)				(at 140 K)
UT.GD109	Standard	0.681	1.04	0.98
GD110	(+15%)	0.634	0.98	0.96
GD111	(-15%)	0.714	1.11	1.12
GD112	H-diluted	0.813	1.16, 1.37	1.16
Group II(UT)				(at 80 K)
L2101	50:50	0.514	1.04	1.04
L2103	45:55	0.674	1.13	1.14
L2102	40:60	0.708	1.18	1.21
Group III(BPSolar)				(at 120 K)
A8128	a-SiGe	0.65	1.06	1.08
A8139	a-SiGe	0.63	1.01	1.07
A8226	a-Si	0.92	1.33	1.24

IV.3. Results:

4.3.1 Comparing PL and EL Spectra in a-SiGe Cells:

The luminescence spectrum obtained at 80 K originates from tail-to-tail transitions, hence it gives information about the optical gap and the energy distribution of the tail states. One may expect the same spectral lineshape for the EL and PL from the same sample. In Figs. 24(a) and 8(b), typical EL and PL spectra at 80 K are shown for a group of cells deposited at T_S=200 ˚C with increasing H dilution from R=25 to 100. Interestingly, we find that the EL peak energy shifts from 1.28 to 1.43 eV and the band width decreases from 294 to 206 meV as shown in Fig. 8(a); whereas, the PL spectral lineshapes do not change much as shown in Fig. 24(b). More interestingly, at the H dilution of R=100 the EL peak energy (1.43 eV) is 20 meV higher than PL's (1.41 eV). To our knowledge, this phenomenon of EL_{peak}>PL_{peak} has not been observed in a-Si based diodes. We observed the same tendency in the three groups of cells listed in Table I. So, we believe that the results can not be due to experimental error.

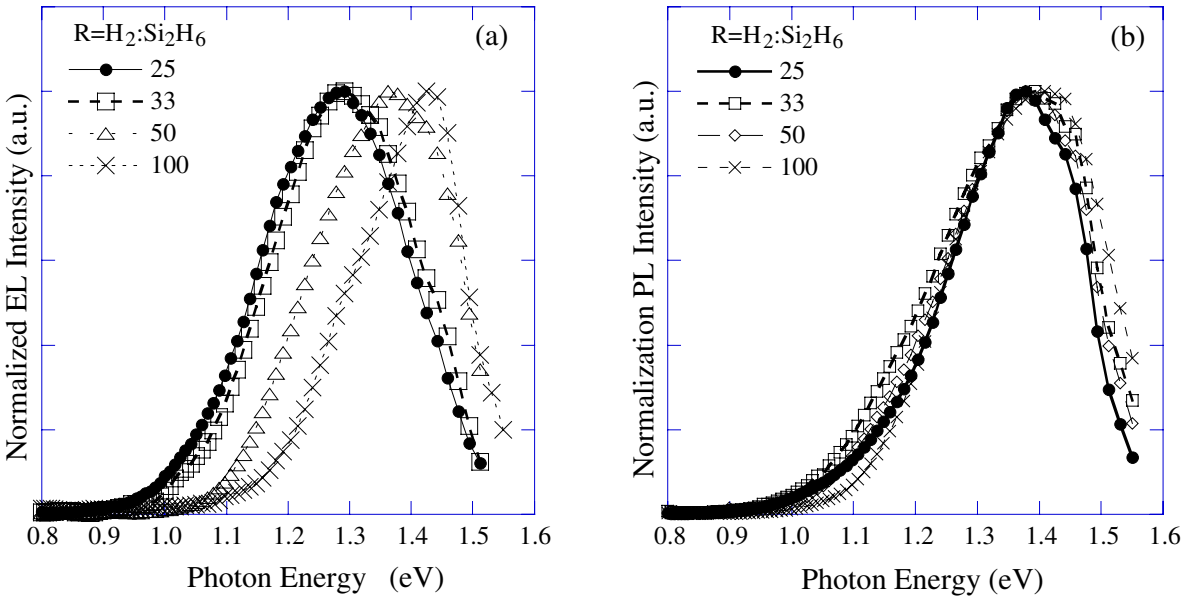

Fig. 24 Typical luminescence spectra for a group of cells deposited at T_S=200 ˚C with different H dilution ratio from R=25 to 100, (a) EL, and (b) PL.

We further studied the EL and PL spectra of a-SiGe cells with different Ge content (the flow ratio of GeH_4:Si_2H_6=45:55, and 50:50). The typical EL and PL spectra from a pair of a-SiGe cells are shown in Figs 25(a) and 25(b), respectively. The result shows that (a) the EL peak energy, EL_{peak}, is the same as the PL_{peak} within the experimental error of 10 meV, and (b) both the EL_{peak} and PL_{peak} decrease from ~1.14 to 1.04 eV with increasing Ge content due to the reduction of the optical gap.

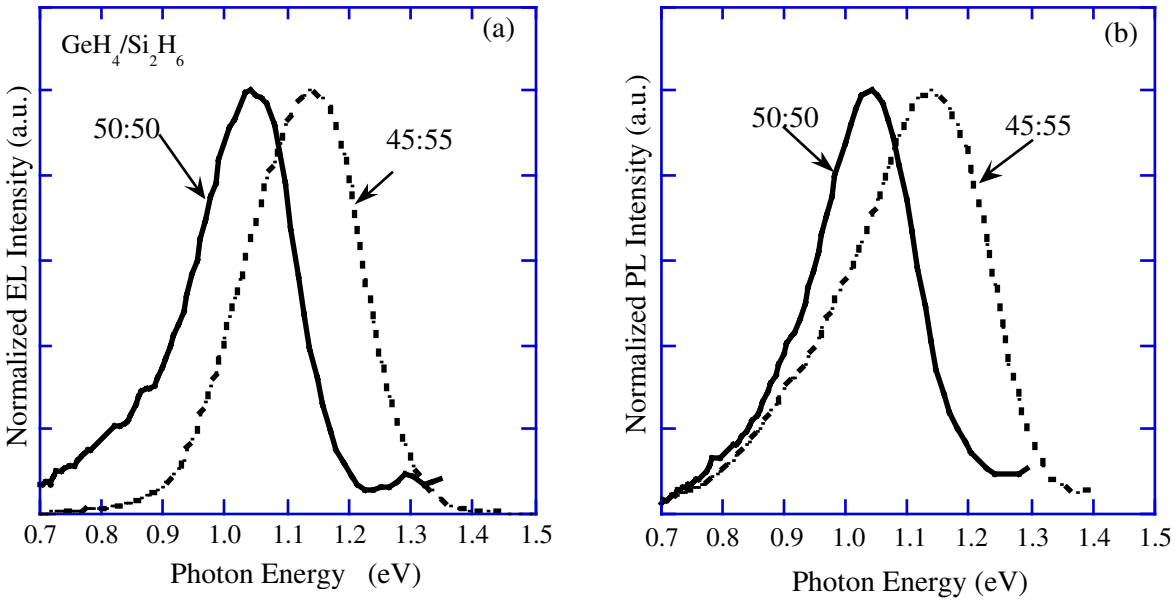

Fig. 25 Typical luminescence spectra for a group of a-SiGe cells with different Ge flow ratio from GeH_4:Si_2H_6=45:55 to 50:50, (a) EL, and (b) PL.

4.3.2 Correlation Between PL/EL Peak Energy Position and V_{oc} in a-SiGe Cells

Table VII lists the PL and EL peak energies and the V_{oc} of the three groups of solar cells made at the Univ. of Toledo and BPSolar. One can see the correlation in Fig. 26.

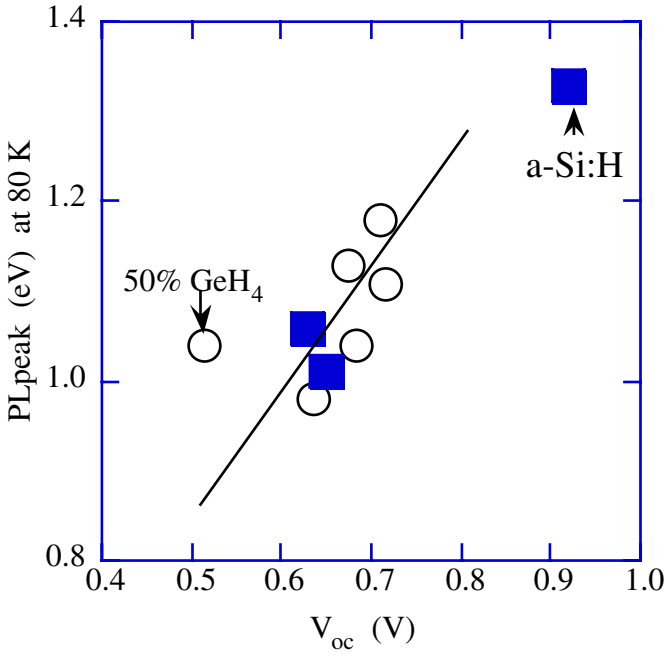

Fig. 26 The peak energy of PL (and EL) from the i-layer is correlated to the V_{oc} in of the samples listed in Table VI.

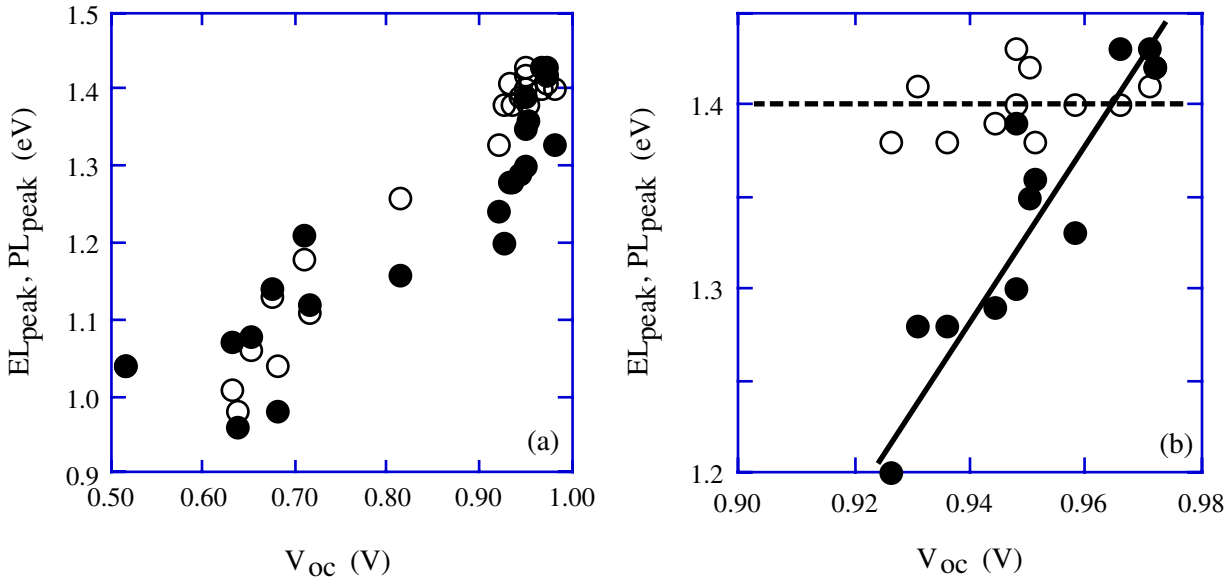

Fig. 27 Correlation between V_{oc} and the EL_{peak}(•) and PL_{peak}(O) at 80 K (a) for a-Si:H and a-SiGe cells, and (b) for a-Si:H cells with different H-dilution.

Finally, we summarize all the data of EL_{peak} and PL_{peak} at 80 K as a function of V_{oc} for all the a-Si:H and a-SiGe cells being studied. In Fig. 27(a), one can see that the higher the luminescence peak energy, the larger the V_{oc} obtained. However, there are two interesting points: First, the EL_{peak} is NOT always less than the PL_{peak} for the same sample. It can be the same or even larger as shown on the right size in Fig. 27(b) (the largest V_{oc}). Second, the EL_{peak} shifts 50 meV from 1.28 to 1.43 eV in the same direction as V_{oc} does; whereas, the PL_{peak} at ~1.4 eV is independent of V_{oc}.

IV.4. Discussion:

Both the luminescence peak energy and the V_{oc} are relevant to the optical gap of the i-layer material, so it is reasonable to observe a correlation between the luminescence peak energy and V_{oc}. The PL feature has been explained by the thermalization model, i.e. the PL_{peak} depends on the position of the demarcation level, E_D. The carrier transport is not involved in PL processes. As long as the optical gap and the band tails have not changed much, the PL lineshape would not change. We explain the differences between the EL_{peak} and PL_{peak} by the dispersive-transport-controlled recombination model. At low temperature (80 K) hopping transport in the exponential band tail must be considered. When the carrier lifetime is longer than its transit time, the carriers would hop down to the transport level, E_t, then recombine. In the case of low H-diluted a-Si:H cells, the carrier recombination lifetime in the i-layer is much longer than the transit time. In other words, E_t is deeper than E_D, hence $PL_{peak} > EL_{peak}$ was observed. However, for a-SiGe cells, the mobility lifetime product ($\mu\tau$) is two or three orders of magnitude less than that for a-Si:H, so the carriers would recombine right after injection into the i-layer. When E_t is equal to E_D, $PL_{peak} = EL_{peak}$ was observed in a-SiGe cells. The carrier lifetime could be further shortened due to an increase of defect density by microcrystallinity in the high-H-diluted cells. Therefore, the energy position of E_t could be higher than E_D, and then $EL_{peak} > PL_{peak}$ was obtained in highly-H-diluted cells.

IV.5. Conclusion:

EL and PL spectroscopies were used to study the effects of H-dilution in a-Si:H as well as the effects of varying Ge content in a-SiGe solar cells. Statistically, the higher the luminescence peak energies, EL_{peak} and PL_{peak}, the larger the V_{oc}. However, the V_{oc} is not only relevant to the optical gap but also to the transport processes. This was demonstrated clearly in the EL spectra. In conclusion:

a. The V_{oc} increased with increasing H dilution. When R increased from 20 to 100, the EL_{peak} shifted from 1.28 to 1.43 eV; whereas PL_{peak} at ~1.40 eV did not change.
b. For a-SiGe p-i-n cells (GeH_4:Si_2H_6=45:55 and 50:50), the peak energy positions of the EL and PL are the same. Both the EL_{peak} and PL_{peak} decreased from ~1.14 to 1.04 eV with increasing Ge content due to the reduction of the optical gap.
c. We observed $EL_{peak} > PL_{peak}$ in highly H-diluted a-Si:H p-i-n cells.

V. NMR investigation in a-Si:H [16-19]

V.1 Introduction:

Until very recently, device quality a-Si:H films prepared by conventional PE-CVD technique in different labs exhibited very little difference in structural and physical properties such as the microstructures of hydrogen distribution as detected by nuclear magnetic resonance (NMR). This situation has changed since the demonstration that a-Si:H produced by the hot-wire technique exhibits improved stability; such high quality a-Si:H contains a very low hydrogen content of 2-3 at.% compared to 8-10 at.% in device quality GD a-Si:H. Moreover, there is growing evidence that hot-wire a-Si:H is very different from the PE materials, including the hydrogen microstructures detected by NMR. The 1H NMR spectrum of a-Si:H consists of two components, a narrow line with a typical full width at half maximum (FWHM) of a few kHz and a broad line with a typical FWHM of 22 - 35 kHz in PE a-Si:H; this broad line is 50 kHz in hot-wire a-Si:H. Clusters of Si-H have been identified as the origin of the broad component in device quality materials. Previous multiple quantum NMR (MQ NMR) studies suggest that the typical number of hydrogen atoms per cluster is 5 - 7 in device quality PE a-Si:H and at least 14 in hot-wire a-Si:H.[29] One of the important issues is the nature of these H clusters.

We use innovative NMR techniques to address a wide range of issues in a-Si:H including the short- and intermediate-range order, nanostructures, distribution of Si-H bonds, and molecular hydrogen. Changes of these properties with sample preparation conditions, annealing, and light soaking could provide valuable information on the metastability of a-Si:H. One of the important progresses of our NMR experiments is the change of approach from measuring a-Si:H powder to measuring a single a-Si:H thin film on a quartz substrate. This was made possible by the development of a sensitive proton-background-free NMR probe. It also allows us to carry out NMR characterization on the same piece of a-Si:H film as other characterizations such as IR, photoluminescence, and photoconductivity.

V.2. Measurement of short- and intermediate-range order:

Theoretical calculations predict that the magnetic susceptibility $|\chi|$ in a-Si:H increases monotonically as a function of local structural disorder including the short- and intermediate-range order. Thus, precise measurement of χ provides short- and intermediate-range structural information that is otherwise difficult to obtain. We have shown that the NMR measurement of χ for a single a-Si:H film can be precise. The NMR resonance frequency measures the local magnetic field H_{local}, given by (in cgs units) $H_{local} = H_0 - N_d M + 4\pi M/3 + H_{micro}$. The first term is the external field, the second term is the so-

called demagnetization field (M= magnetization density) where the factor N_d depends on the sample shape and the orientation of the sample with respect to the external field. The third term is the Lorentz cavity surface dipole field, and the last term H_{micro} is the contribution from inside the Lorentz cavity. Contributions from inside the spherical mesoscopic Lorentz cavity (e.g., magnetic dipoles, chemical shift, etc.) lead to a powder pattern in the case of an amorphous sample and is independent of sample orientation with respect to the external field. The shift of the NMR frequency σ (in ppm) due to the susceptibility (or M) effect is given by $\sigma = (4\pi/3 - N_d)\,\chi \times 10^6$ where χ is the volume susceptibility. It can be shown that $N_d = 4\pi\cos^2\theta$ for a thin slab such as the a-Si:H thin film where θ is the angle between the film's normal axis and the external magnetic field direction. Figure 28 shows the proton spectra of a conventional a-Si:H film at $\theta = 0°$ and $\theta = 72°$.

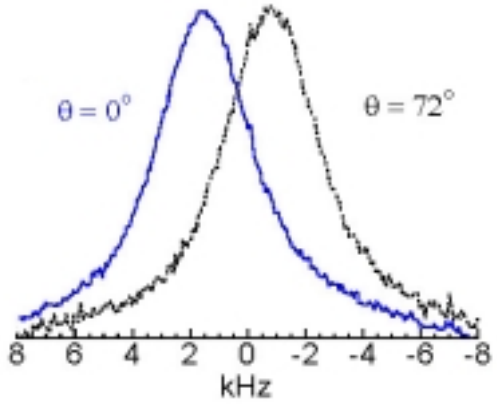

Fig. 28 Proton NMR spectra of conventional PECVD a-S:H at two different orientation. Only the narrow component is displayed. The broad component extends outside this scale.

The Lorentzian peak of about 4 kHz in width is due to relatively isolated Si-H bonds, a fact that has been well known for a long time. The shift of the peak position with angle θ is as expected from the susceptibility effect, and the lineshape does not change with θ because the film is amorphous. From this experiment, the magnetic susceptibility can be measured precisely. Table VIII lists the measured χ for three samples. Clearly, conventional PECVD has the largest $|\chi|$ value, high H-dilution PECVD is in between, and HW a-Si:H films have the smallest $|\chi|$ value. Thus, there seems to be a correlation between $|\chi|$, thus the short- and medium-range order, and the metastability.

Table VIII lists the measured χ for three samples

Sample	$-\chi$ ($\times 10^{-6}$, cgs units)	$-\chi_M$ ($\times 10$ cm^3/mol)	Mass density ρ (g/cm^3)	Substrate T (°C)	Thickness (microns)
Standard PECVD	1.06 ± 0.02	13.5 ± 0.3	2.20 ± 0.02	200	~ 5
High-H-dilution PECVD	0.96 ± 0.03	12.1 ± 0.4	2.24 ± 0.02	250	0.5
High-growth-rate HW (55 Å/s)	0.92 ± 0.03	11.5 ± 0.3	2.25 ± 0.01	~ 370	2.2

V.3. Nanostructures:

The structure of a-Si:H is not completely homogeneous. The NMR measurement shows that Si-H bond distribution has two components, dilute Si-H and clustered Si-H bonds. In addition, there are voids on nanometer scales. Recently, we discovered an interesting feature of high growth rate HWCVD a-Si:H, namely, the presence of imbedded nano-channels perpendicular to the film surface. These nano-channels are filled with high pressure H_2 gas of several hundred atmospheres during sample growth. The system is illustrated in Fig. 29.

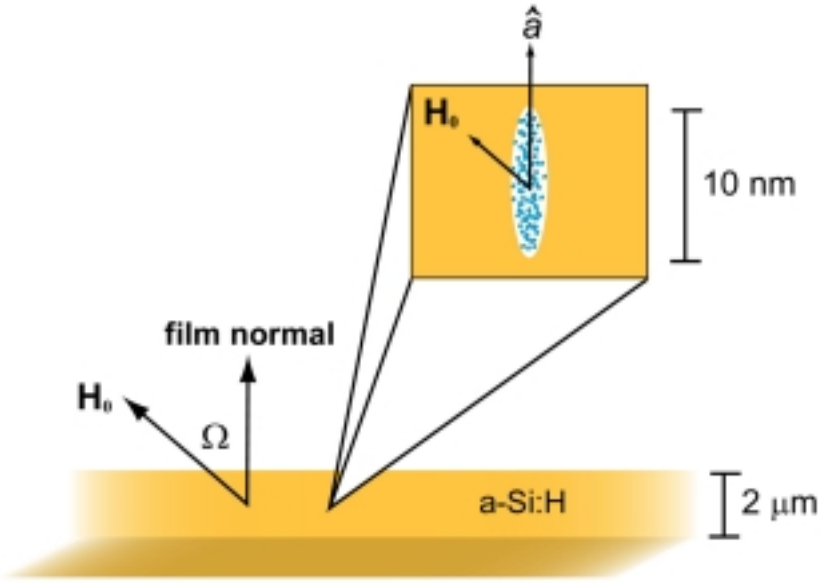

Fig. 29 Illustration of the side view of an a-Si:H film (about 1 μm thick) on substrate (quartz) containing nano-channels (white columns) filled with high pressure H_2 gas (blue dots).

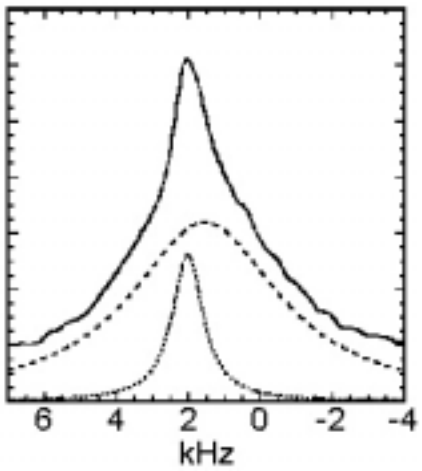

Fig.30 Narrow-peak spectrum of a high-H-dilution PECVD film taken at θ =0°. Dotted lines are the line-fits. The broad line is outside the scale. The 4 kHz line is the conventional narrow line due to diluted Si-H bonds. The very narrow line is the H_2 peak.

Direct observation of the molecular hydrogen peak is common in high H-diluted PECVD and HWCVD a-Si:H single film on substrate. An example is shown in Fig. 30 where the narrow region of the proton spectrum for a high H-diluted PECVD film is shown. The H_2 peak is clearly visible. Similar spectra are observed in HWCVD a-Si:H films grown at high growth rate. Here, a narrow peak of less than 1 kHz in width is observed in addition to the Si-H peak. The two-peak simulations of the spectra are shown in Fig. 14. Based on the measurement of void volume fraction (a few percent) in such HWCVD a-Si:H film as determined by the density and small-angle-x-ray scattering (SAXS) measurements and the total amount of H_2 based on NMR measurement, the average pressure inside the voids is estimated to be ~1.1 kbar.

What is surprising is that the linewidth of the H_2 peak as can be seen clearly in Fig. 31, depends on the angle θ in contrast to the expectation of the isotropic behavior in amorphous systems. Furthermore, the H_2-peak susceptibility shift is also different from the bulk value effect as represented by the behavior of the Si-H peak. This shows that the structure of such HWCVD a-Si:H is not isotropic on microscopic scales.

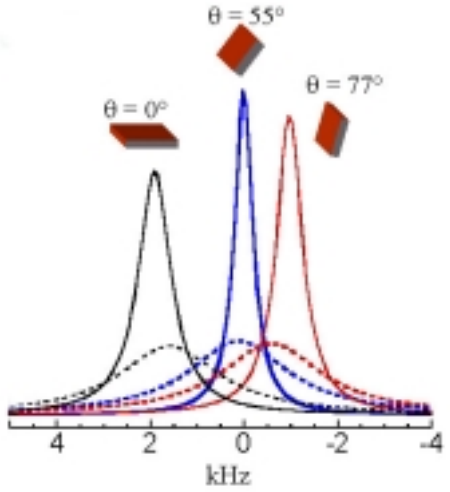

Fig. 31 Simulations of the proton NMR spectra at three different orientations of HWCVD a-Si:H grown at high rate.

In fact, the angle-dependent linewidth is due to residual dipole-dipole interactions between H_2 molecules that appear as an effect of nano-confinement. Figure 32 shows the measured $1/\pi T_2$ versus the angle θ as well as the linewidth versus θ. Clearly, the linewidth is almost exclusively accounted for by the transverse relaxation rate $1/T_2$. The angle dependence of linewidth follows the formula

$$Linewidth = 280Hz\,|\cos^2\vartheta - 1\,| + 450Hz$$

which is exactly what is expected from a system of interacting dipoles aligned along the channels perpendicular to the film. Quantitative calculations show that such angle-dependence arises from nano-channels ~ 1nm in diameter and the length is about 5 times longer. The shift is also in agreement with the local susceptibility shift in such elongated, aligned voids.

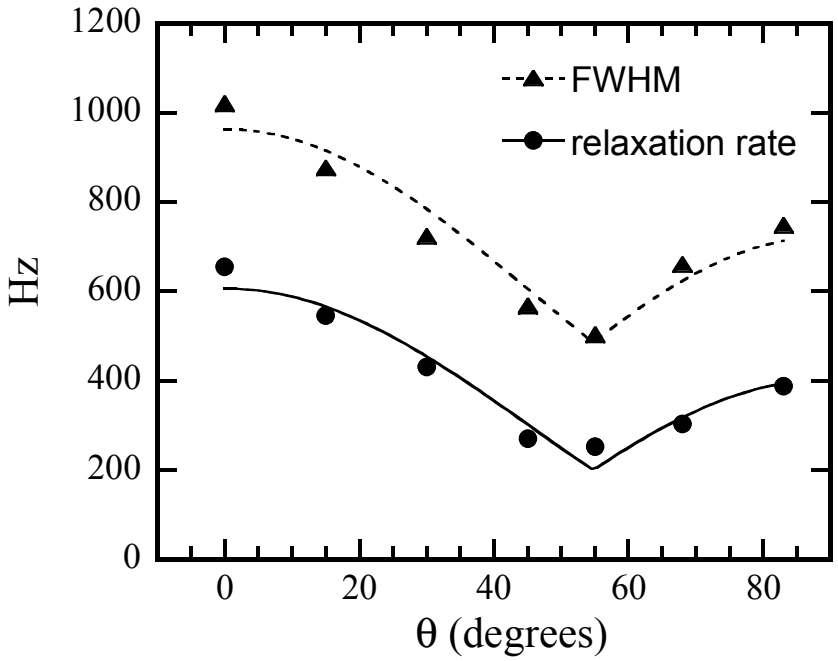

Fig. 32 Linewidth and spin-spin relaxation rate $1/\pi T_2$ of the narrow proton peak in HWCVD a-Si:H grown at high rate versus the angle θ.

V.4. Conclusions

Improved structural order has been detected in a-Si:H films deposited by PECVD with high H-dilution and by HWCVD directly via magnetic susceptibility. Structural improvement may be directly related to the broad NMR linewidth through its effect on the degree of relaxation of the hydrogenated multivacancy H clusters. The appearance of nanostructure, namely aligned voids with diameters on the scale 1 nanometer, filled with dense H_2 gas, may be a further by-product of better overall structural ordering in the film.

FURTHER EFFORTS

We have completed the three phases and the extension period of the research project and met the project goal. Efforts will be continued to cooperate with team members, especially members from the PV industry to study the factors governing the SWE in a-Si:H solar cells. In the renewed subcontract period, we will pay more attention to the V_{oc} in relation to the i-layer properties, high growth rate and SiGe cells using the PL spectroscopy which give more direct useful information to thin film PV performance; also search for the link between photo-induced structural- and electronic degradations.

Publications:

1. Light-induced Structural Changes and their Correlation to Conductivity Changes in Intrinsic Hydrogenated Amorphous Silicon Films, Daxing Han, Jonathan Baugh, Guozhen Yue, and Qi Wang, Phys. Rev. B **62**, 7169 (2000).
2. Structural Ordering and its Correlation to the Optoelectronic Properties of a-Si:H Films, Jonathan Baugh, Daxing Han, Alfred Kleinhammes, Qi Wang, and Yue Wu, NCPV Program Review Meeting, (April, 2000, Dever,CO).
3. Photo-induced Structure Metastability and the SWE in a-Si:H, Daxing Han, Tamihiro Gotoh, Motoi Nishio, Tomonari Sakamoto, Shuichi Nonomura, Shoji Nitta, Qi Wang, Eugene Iwaniczko, Harv Mahan, NCPV Photovoltaics Program Review Proceeding of the 15th Conference, p.260 (editor Mowafak Al-Jassim, John P. Thornton, James M. Gee, Denver, 1998).
4. Light-induced Change of Si-H Bond Absorption in Hydrogenated Amorphous Silicon, Guozhen Yue, Jonathan Baugh, Liangfan Chen, Qi Wang, Eugene Iwaniczko, Guanglin Kong, Yue Wu, Daxing Han, Amorphous Silicon Technology-1998, MRS Symposium Proc. **507** 685-690 (1998).
5. Photoluminescence and Raman Studies in Thin Film Materials: Transition from Amorphous to Microcrystalline Silicon,Guozhen Yue, J. D. Lorentzen, Jing Lin, Qi Wang and Daxing Han, Appl. Phys. Lett. **75**, 492 (1999).
6. Structure and optoelectronic properties as a function of hydrogen-dilution of microcrystalline silicon films deposited by hot wire chemical vapor deposition, Guozhen Yue, Jing Lin, Qi Wang and Daxing Han, Amorphous and Heterogeneous Silicon Thin Films-Fundamentals to Devices, MRS Symposium, Proc. **557**, 525-530 (1999).
7. Microcrystalline silicon films deposited by hot wire chemical vapor deposition, Daxing Han, Guozhen Yue, and Qi Wang, Procedings of The Japan-China Bilateral Symposium on Advanced Materials Engineering, 109-114 (March 17-19, 1999, Tokyo, Japan).
8. Optical and electronic properties of microcrystalline silicon as a function of microcrystallinity, Daxing Han, Guozhen Yue, J. D. Lorentzen, Jing Lin, H. Habuchi, and Qi Wang, J.Appl. Phys. **87**, 1882 (2000).
9. Optical and electronic properties of microcrystalline silicon deposited by hot-wire CVD, Daxing Han, H. Habuchi, T. Hori, A. Nishibe, T. Namioka, Jing Lin and Guozhen Yue, J. Non-Cryst. Solid, **266/269**, 274-278 (2000).
10. Characteristics of the Low Energy Photoluminescence in μc-Si Films, Guozhen Yue, Laurie E. McNeil and Daxing Han, Qi Wang, J. Appl. Phys. **88**, 4940 (2000).
11. Electronic states of intrinsic layers in n-i-p solar cells near amorphous to microcrystalline silicon transition studied by photoluminescence spectroscopy, Guozhen Yue, Daxing Han, D.L. Williamson, Jeffrey Yang, Kenneth Lord and Subhendu Guha, Appl. Phys. Lett. **77**, 3185 (2000).
12. Characterization for the Onset of Crystallization of Amorphous to Microcrystalline Silicon by Optical Spectroscopies, Guozhen Yue, Daxing Han, G. Ganguly, Qi Wang, Jeffrey Yang, and Subhendu Guha, NCPV Program Review Meeting, (April, 2000, Dever,CO).
13. Effects of Hydrogen Dilution on a-Si:H and its Solar Cells Studied by Raman and Photoluminescence Spectroscopy, Guozhen Yue, Jessica M. Owens, Jennifer Weinberg-Wolf, Daxing Han, Jeffrey Yang, Kenneth Lord, Boajie Yan, and Subhendu Guha, MRS Symposium Proc A9.7 (2001).
14. Thickness and Interface Layer Effects on The Amorphous Silicon Film Property Studied by Various Photoluminescence Excitation Wave Lengths, Guozhen Yue, Daxing Han, Jeffrey Yang, and Subhendu Guha, Amorphous Silicon Technology-1998, MRS Symposium Proc **609**, A5.9 (2000).
15. Electro- and photo-luminescence spectra from a-Si:H and a-SiGe p-i-n solar cells, Guozhen Yue, Xunming Deng, G. Ganguly, and Daxing Han, J. Non-Cryst. Solid, **266/269**, 1119-1123 (2000).
16. Magnetic Susceptibility and Microstructure of Hydrogenated Amorphous Silicon Measured by Nuclear Magnetic Resonance on a Single Thin Film, J. Baugh, D.X. Han, A. Kleinhammes1, and Y. Wu, Appl. Phys. Lett. **78**, 466 (2001).

17. Diamagnetic Susceptibility of Micron Thick a-Si:H Films Measured Via Proton NMR: A Probe of Structual Order, Jonathan Baugh, Daxing Han, Qi Wang and Yue Wu, Amorphous Silicon Technology-1998, MRS Symposium Proc **609**, A16.3**609**, A5.9 (2000).
18. Microstructure and dynamics of hydrogen in a-Si:H studied by NMR, Jonathan Baugh, Daxing Han, Alfred Kleinhammes, Chunlei Liu, and Yue Wu, Qi Wang, J. Non-Cryst. Solid, **266/269**, 185-189 (2000).
19. Proton NMR and Magnetic Susceptibility in a-Si:H, Jonathan Baugh, Daxing Han, Alfred Kleinhammes, and Yue Wu, MRS Symposium Proc -A27.4 (2001).
20. Large Red Shift of PL Peak Energy in High Growth Rate a-Si:H Prepared by Hot-Wire CVD, Daxing Han, Guozhen Yue, Jennifer Weinberg-Wolf and Jessica M. Owens Yueqin Xu and Qi Wang, MRS Symposium Proc -A7.4 (2001).
21. Model of Hydrogen-Mediated Metastable Changes in a Two-Domain Amorphous Silicon Network, Jonathan Baugh and Daxing Han, MRS Symposium Proc -A19.1 (2001).
22. Electronic States and the Light-Induced Metastable Effects in Hydrogenated Amorphous Silicon Prepared by Hot-Wire CVD, Daxing Han, Guozhen Yue, H. Habuchi, Eugene Iwaniczko, Qi Wang, Thin Solid Films, **395**, 134-137 (2001).
23. Localized electronic states related to O_2 intercalation and photoirradation on C_{60} films and C_{70} films, Hitoe Habuchi, Shoji Nitta, Daxing Han and Shuichi Nonomura, J. Appl. Phys. **12**, 8580 (2000).
24. Phtodegradation in a-Si:H Prepared by Hot-Wire CVD as a function of Substrate and Filament Temperatures, Daxing Han, Guozhen Yue, Jing Lin, Eugene Iwaniczko, Qi Wang, MRS Symposium Proc **609**, A22.7 (2000).
25. A combinatorial study of materials in transition from amorphous to microcryatalline silicon, Qi Wang, Guozhen Yue, Jing Lin, and Daxing Han, Solid State Communications **113**, 175-178 (2000).
26. Structural Changes and Mobile Hydrogen in a-Si:H Observed by Proton NMR, Jonathan Baugh, Daxing Han, Qi Wang and Yue Wu, Amorphous and Heterogeneous Silicon Thin Films-Fundamentals to Devices, MRS Symposium, Proc. **557**, 383-388 (1999).
27. Internal Electric Field Profile of a-SiGe p-i-n Solar Cells, Xinhua Geng, Xunming Deng, Qi Wang, and Daxing Han, Amorphous Silicon Technology-1998 (MRS Symposium Proc. **507**, 187-192 (1998).

References:

1. Daxing Han, Jonathan Baugh, Guozhen Yue, and Qi Wang, Phys. Rev. B **62**, 7169 (2000).
2. Jonathan Baugh, Daxing Han, Alfred Kleinhammes, Qi Wang, and Yue Wu, NCPV Program Review Meeting, (April, 2000, Dever,CO).
3. Daxing Han, Tamihiro Gotoh, Motoi Nishio, Tomonari Sakamoto, Shuichi Nonomura, Shoji Nitta, Qi Wang, Eugene Iwaniczko, Harv Mahan, NCPV Photovoltaics Program Review Proceeding of the 15th Conference, p.260 (editor Mowafak Al-Jassim, John P. Thornton, James M. Gee, Denver, 1998).
4. Guozhen Yue, Jonathan Baugh, Liangfan Chen, Qi Wang, Eugene Iwaniczko, Guanglin Kong, Yue Wu, Daxing Han, Amorphous Silicon Technology-1998, MRS Symposium Proc. **507** 685-690 (1998).
5. Guozhen Yue, J. D. Lorentzen, Jing Lin, Qi Wang and Daxing Han, Appl. Phys. Lett. **75**, 492 (1999).
6. Guozhen Yue, Jing Lin, Qi Wang and Daxing Han, Amorphous and Heterogeneous Silicon Thin Films-Fundamentals to Devices, MRS Symposium, Proc. **557**, 525-530 (1999).
7. Daxing Han, Guozhen Yue, and Qi Wang, Procedings of The Japan-China Bilateral Symposium on Advanced Materials Engineering, 109-114 (March 17-19, 1999, Tokyo, Japan).
8. Daxing Han, Guozhen Yue, J. D. Lorentzen, Jing Lin, H. Habuchi, and Qi Wang, J.Appl. Phys. **87**, 1882 (2000).
9. Daxing Han, H. Habuchi, T. Hori, A. Nishibe, T. Namioka, Jing Lin and Guozhen Yue, J. Non-Cryst. Solid, **266/269**, 274-278 (2000).
10. Guozhen Yue, Laurie E. McNeil and Daxing Han, Qi Wang, J. Appl. Phys. **88**, 4940 (2000).
11. Guozhen Yue, Daxing Han, D.L. Williamson, Jeffrey Yang, Kenneth Lord and Subhendu Guha, Appl. Phys. Lett. **77**, 3185 (2000).
12. Guozhen Yue, Daxing Han, G. Ganguly, Qi Wang, Jeffrey Yang, and Subhendu Guha, NCPV Program Review Meeting, (April, 2000, Dever,CO).
13. Guozhen Yue, Jessica M. Owens, Jennifer Weinberg-Wolf, Daxing Han, Jeffrey Yang, Kenneth Lord, Boajie Yan, and Subhendu Guha, MRS Symposium Proc -2001. (in press).
14. Guozhen Yue, Daxing Han, Jeffrey Yang, and Subhendu Guha, Amorphous Silicon Technology-1998, MRS Symposium Proc **609**, A5.9 (2000).
15. Guozhen Yue, Xunming Deng, G. Ganguly, and Daxing Han, J. Non-Cryst. Solid, **266/269**, 1119-1123 (2000).
16. J. Baugh, D.X. Han, A. Kleinhammes1, and Y. Wu, Appl. Phys. Lett. **78**, 466 (2001).
17. Jonathan Baugh, Daxing Han, Qi Wang and Yue Wu, Amorphous Silicon Technology-1998, MRS Symposium Proc **609**, A16.3**609**, A5.9 (2000).
18. Jonathan Baugh, Daxing Han, Alfred Kleinhammes, Chunlei Liu, and Yue Wu, Qi Wang, J. Non-Cryst. Solid, **266/269**, 185-189 (2000).
19. Jonathan Baugh, Daxing Han, Alfred Kleinhammes, and Yue Wu, MRS Symposium Proc -A27-4 (2001).
20. D.L. Staebler and C.R.Wronski, Appl. Phys. Lett. **31**, 292 (1977).
21. M. Stutzmann, W. B. Jakson, and C. C. Tsai, Phys. Rev. **B32**, 23 (1985).
22. H. M. Branz, Sally Asher, H. Gleskova and S. Wagner, Phys. Rev. **B59**, 5513 (1999).
23. Yiping Zhao, Guanglin Kong, Guangqin Pan, and Xianbo Liao. Phys. Rev. Lett. **74**, 558 (1995).
24. T. Gotoh, S. Nonomura, M.Nishio, S. Nitta, M. Kondo and A. Matsuda, Appl. Phys. Lett.**72**, 2978 (1998).
25. R. Biswas, Y.P. Li , Phys. Rev. Lett. **82**, 2512 (1999).
26. D.V. Tsu, B.S. Chao, S.R. Ovshinsky, S. Guha and J. Yang, Appl. Phys. Lett., **71**, 1317, (1997).
27. L. Yang and L. Chen, Appl. Phys. Lett. **63**, 400 (1993).
28. A.H. Mahan, J. Carapella, B.P. Nelson, R.S. Crandall, and I. Balberg, J.Appl. Phys. **69**, 6728 (1991).

29. Y. Wu, J. T. Stephen, Daxing Han, J. M. Rutland, R.S. Crandall, and A. H. Mahan, Phys. Rev. Lett. **77**, 2049 (1996).
30. Xiao Liu, B. E. White, Jr., and R. O. Pohl, E. Iwanizcko, K. M. Jones, A. H. Mahan, B. N. Nelson, R. S. Crandall, and S. Veprek, Physical Review Letters, **78**, 4418 (1997).
31. Jonathan Baugh's Ph.D. thesis, UNC-CH, (Dec. 2001).
32. D. Redfield and R.H. Bube, Appl. Phys. Lett. **54**, 1037 (1989).
33. Daxing Han, Guozhen Yue, H. Habuchi, Eugene Iwaniczko, Qi Wang, Thin Solid Films, **395**, 134-137 (2001).
34. I. Kaiser, N. H. Nickel, W. Fuhs, and W. Pilz, Phys. Rev. B **58**, R1718 (1998).
35. Daxing Han, Changhua Qiu, and Wenhao Wu, *Phil. Mag*. **B54**, L9-L13 (1986).

Abstract

This report describes continuing studies on photoluminescence (PL) electroluminescence (EL), Raman, and NMR by UNC-CH during the three years and the extension period. Systematic studies on the transition materials and their solar cells and a review of the photo-induced structural changes in correlation to the electronic degradation have led to better understanding of the factors determining the photodegradation in a-Si:H solar cells.

THE UNIVERSITY OF NORTH CAROLINA
AT
CHAPEL HILL

The University of North Carolina at Chapel Hill
Department of Physics and Astronomy
Chapel Hill, N.C. 27599-3255

CB# 3255, Phillips Hall
Tel: (919) 962-5002
FAX: (919) 962-0480

Jan. 24, 2002
Dr. Bolko von Roedern
NREL
1617 Cole Blvd.
Golden, CO 80401

Dear Bolko,

Here is the revised Final Technical Report of 28/1/98-08/15/01 on the NREL Subcontract No XAK-8-17619-11, with University of North Carolina at Chapel Hill. A disc is included (Microsoft Word, Macintosh).

Sincerely,

Daxing Han

cc: Carolyn Lopez (NREL)
Donna Braxton (UNC)

REPORT DOCUMENTATION PAGE

Form Approved
OMB NO. 0704-0188

1. AGENCY USE ONLY (Leave blank)	2. REPORT DATE	3. REPORT TYPE AND DATES COVERED
	March 2002	Final Subcontract Report, 28 January 1998 – 15 August 2001

4. TITLE AND SUBTITLE
Search for the Factors Determining the Photodegradation in High Efficiency a-Si:H Solar Cells, Final Subcontract Report, 28 January 1998 – 15 August 2001

5. FUNDING NUMBERS
CF: XAK-8-17619-11
PVP25001

6. AUTHOR(S)
Daxing Han

7. PERFORMING ORGANIZATION NAME(S) AND ADDRESS(ES)
University of North Carolina
Chapel Hill, North Carolina

8. PERFORMING ORGANIZATION REPORT NUMBER

9. SPONSORING/MONITORING AGENCY NAME(S) AND ADDRESS(ES)
National Renewable Energy Laboratory
1617 Cole Blvd.
Golden, CO 80401-3393

10. SPONSORING/MONITORING AGENCY REPORT NUMBER
NREL/SR-520-31754

11. SUPPLEMENTARY NOTES
NREL Technical Monitor: Bolko von Roedern

12a. DISTRIBUTION/AVAILABILITY STATEMENT
National Technical Information Service
U.S. Department of Commerce
5285 Port Royal Road
Springfield, VA 22161

12b. DISTRIBUTION CODE

13. ABSTRACT *(Maximum 200 words):* This report describes continuing studies on photoluminescence (PL), electroluminescence (EL), Raman, and nuclear magnetic resonance (NMR) by the University of North Carolina-Chapel Hill during the three years and the extension period. Systematic studies on the transition materials and their solar cells and a review of the photo-induced structural changes in correlation to the electronic degradation have led to better understanding of the factors determining the photodegradation in a-Si:H solar cells. NHR established significant differences, as in the bonding of hydrogen in the hot-wire- and plasma-deposited amorphous silicon.

14. SUBJECT TERMS: PV; amorphous silicon; a-Si:H; photoluminescence; electroluminescence; Raman spectroscopies; nuclear magnetic resonance; photodegradation

15. NUMBER OF PAGES

16. PRICE CODE

17. SECURITY CLASSIFICATION OF REPORT	18. SECURITY CLASSIFICATION OF THIS PAGE	19. SECURITY CLASSIFICATION OF ABSTRACT	20. LIMITATION OF ABSTRACT
Unclassified	Unclassified	Unclassified	UL